Advanced Materials

Metal Organic Framework (MOF) derived Electrodes with Robust and Fast Lithium Storage for Li-Ion Hybrid Capacitors

--Manuscript Draft--

Manuscript Number:	adma.201807830
Full Title:	Metal Organic Framework (MOF) derived Electrodes with Robust and Fast Lithium Storage for Li-Ion Hybrid Capacitors
Article Type:	Communication
Section/Category:	
Keywords:	MOF-derived Materials, manganese oxide, Li-ion capacitors, Energy Storage, Energy Density.
Corresponding Author:	Roland A. Fischer Technische Universität München Garching, GERMANY
Additional Information:	
Question	**Response**
Please submit a plain text version of your cover letter here.	To Dear Editor, We would like to submit our manuscript “Metal Organic Framework (MOF) derived Electrodes with Robust and Fast Lithium Storage for Li-Ion Hybrid Capacitors to Advance Materials as a communication. All authors have read and approved the submitted manuscript. The contents of our manuscript are original and not under consideration for publication elsewhere. Many papers promise electrode materials with energy densities much larger than those of supercapacitors and power densities much greater than those of batteries. However, High energy density AND high power density at the same time, all at a low cost is the real challenge. That is the holy grail of energy storage. Our report delivers precisely that. We are presenting a novel combination featuring simultaneously power density values typical of supercapacitors with energy density values worthy of batteries. This valuable combination has been made possible thanks to the implementation of kinetically-balanced two different Metal Organic Framework (MOF) derived electrodes. A concept most frequently overlooked in hybrid energy storage devices in general and in Lithium-Ion Capacitors (LICs) in particular. Herein, we engineer a well-organized interleaved composite of graphene-like nanosheets decorated with MnO2 nanoparticles (MnO2@C-NS) using manganese-based metal-organic framework (MOF) as a promising anode material for LICs. This uniquely architecture hybrid showed intriguing electrochemical properties including high reversible specific capacity 1054 mAh/g (close to the theoretical capacity of MnO2, 1232 mAh/g) with remarkable rate capability and cyclic stability (90 % over 1000 cycles). Moreover, a novel Li-ion hybrid capacitor (LIHC) is assembled using MnO2@C-NS as anode and MOF derived ultrathin nanoporous carbon nanosheets (derived from other potassium-based metal-organic framework) as cathode materials. The full-cell exhibits ultrahigh specific energy density of 166 Wh/kg at 550 W/kg and maintained to 49.2 Wh/kg even at high specific power density of 3.5 kW/kg as well as long cycling stability (91% over 5000 cycles). The present results already overcome power limits of batteries and energy density limits of Supercapacitors. This is first “Full MOF-derived LIHC” where both anode and cathode are derived from two different MOFs. Both electrodes are different types of easily scalable MOF-derived

	materials with a great potential for low-cost upon mass production. We believe this report is more than just one step forward to the general use of electrochemical energy storage for EVs and stationary applications. By showing the way through engineering LIHC based on MOF derived hybrid materials, enable new opportunities for designing newly advanced MOF derived electrodes for next-generation energy storage devices. We really look forward to the publication of this thorough work in Advance Materials, which we consider the best suited journal for a status-breaking work like the one you have at hand. Sincerely yours and behalf of all coauthors Prof. Dr. Roland A. Fischer Chair of Inorganic and Metal-Organic Chemistry Technical University of Munich and Prof. Dr. Radek. Zboril Regional Centre of Advanced Technologies and Materials, Faculty of Science, Palacky University.
Do you or any of your co-authors have a conflict of interest to declare?	No. The authors declare no conflict of interest.
Corresponding Author Secondary Information:	
Corresponding Author's Institution:	Technische Universität München
Corresponding Author's Secondary Institution:	
First Author:	Roland A. Fischer
First Author Secondary Information:	
Order of Authors:	Roland A. Fischer
	Deepak P. Dubal
	Kolleboyina Jayaramulu, PhD
	Sunil Janaky
	Štěpán Kment
	Pedro Gomez-Romero, Professor
	Chandrabhas Narayana, Professor
	Radek Zbořil
Order of Authors Secondary Information:	
Abstract:	Hybrid inorganic-organic porous metal-organic frameworks (MOFs) demonstrated a great promise as ideal electrode materials for energy-related applications viz. Li-ion batteries and Li-ion Capacitors (LICs). Herein, we engineer a well-organized interleaved composite of graphene-like nanosheets decorated with MnO2 nanoparticles (MnO2@C-NS) using manganese-based MOF as a promising anode

	material for LIHC. This uniquely architecture hybrid showed intriguing electrochemical properties including high reversible specific capacity 1054 mAh/g (close to the theoretical capacity of MnO_2, 1232 mAh/g) at 0.1 A/g with remarkable rate capability and cyclic stability (90% over 1000 cycles). Such a remarkable performance might be assigned to the hierarchical porous ultrathin carbon nanosheets and tightly attached MnO_2 nanoparticles, which provide structural stability and low contact resistance during repetitive lithiation/delithiation processes. Moreover, a novel Li-ion hybrid capacitor (LIHC) is assembled using MnO_2@C-NS as anode and MOF derived ultrathin nanoporous carbon nanosheets (derived from other potassium-based metal-organic framework) as cathode materials. The full-cell exhibits ultrahigh specific energy density of 166 Wh/kg at 550 W/kg and maintained to 49.2 Wh/kg even at high specific power density of 3.5 kW/kg as well as long cycling stability (91% over 5000 cycles). This work shows that engineering MOF derived hybrid materials can significantly impact the Li-ion storage properties.

DOI: 10.1002/((please add manuscript number))
Article type: Communication

Metal Organic Framework (MOF) derived Electrodes with Robust and Fast Lithium Storage for Li-Ion Hybrid Capacitors

Deepak P. Dubal,[1,4*$] Kolleboyina Jayaramulu,[2,3*$] Sunil Janaky,[5] Štěpán Kment,[3] Pedro Gomez-Romero,[4] Chandrabhas Narayana,[5] Radek Zbořil[3*] and Roland A. Fischer[2*]

[1]Dr. D. P. Dubal
School of Chemical Engineering, The University of Adelaide,
Adelaide, South Australia 5005, Australia
Email: dubaldeepak2@gmail.com

[2]Dr. K. Jayaramulu, Prof. Dr. R. A. Fischer
Chair of Inorganic and Metal-Organic Chemistry, Department of Chemistry and Catalysis Research Centre, Technical University of Munich, 85748 Garching, Germany
Email: jaya.kolleboyina@tum.de
Email: roland.fischer@tum.de

[3]Dr. K. Jayaramulu, Dr. S. Kment, Prof. Dr. R. Zboril
Regional Centre of Advanced Technologies and Materials,
Faculty of Science, Palacky University, Šlechtitelů 27, 783 71, Olomouc, Czech Republic.
Email: radek.zboril@upol.cz

[4]Dr. D. P. Dubal, Prof. Dr. P. Gomez-Romero
Catalan Institute of Nanoscience and Nanotechnology (ICN2), CSIC and the Barcelona Institute of Science and Technology, Campus UAB, Bellaterra 08193, Barcelona, Spain

[5]Prof. Dr. C. Narayana, Ms. S. Janaky
Chemistry and Physics of Materials Unit,
Jawaharlal Nehru Centre for Advanced Scientific Research (JNCASR)
Jakkur, Bangalore, 560064, India

[$]Both authors contributed equally.

Keywords: MOF-derived Materials, manganese oxide, nanoporous carbon, Li-ion capacitors, Energy Storage, Energy Density.

Abstract

Hybrid inorganic-organic porous metal-organic frameworks (MOFs) demonstrated a great promise as ideal electrode materials for energy-related applications viz. Li-ion batteries and Li-ion Capacitors (LICs). Herein, we engineer a well-organized interleaved composite of graphene-like nanosheets decorated with MnO_2 nanoparticles (MnO_2@C-NS) using manganese-based metal-organic framework (MOF) as a promising anode material for LIHC. This uniquely architecture hybrid showed intriguing electrochemical properties including high reversible specific capacity 1054 mAh/g (close to the theoretical capacity of MnO_2, 1232 mAh/g) at 0.1 A/g with remarkable rate capability and cyclic stability (90 % over 1000 cycles). Such a remarkable performance might be assigned to the hierarchical porous ultrathin carbon nanosheets and tightly attached MnO_2 nanoparticles, which provide structural stability and low contact resistance during repetitive lithiation/delithiation processes. Moreover, a novel Li-ion hybrid capacitor (LIHC) is assembled using MnO_2@C-NS as anode and MOF derived ultrathin nanoporous carbon nanosheets (derived from other potassium-based metal-organic framework) as cathode materials. The full-cell exhibits ultrahigh specific energy density of 166 Wh/kg at 550 W/kg and maintained to 49.2 Wh/kg even at high specific power density of 3.5 kW/kg as well as long cycling stability (91% over 5000 cycles). This work shows that engineering MOF derived hybrid materials and introducing conductive carbon nanostructure can significantly impact the Li-ion storage properties, enabling new opportunities for designing newly advanced MOF derived electrodes for next-generation energy storage devices.

Introduction

A swift advancement in portable electronics, hybrid electric vehicles, and large-scale smart grids demanding for innovative electrochemical energy storage systems with both high energy and power density as well as long cycle life at low cost.[1-4] In this context, a new system called "Lithium Ion Capacitors (LICs)" is proposed in the beginning of 21st century, which is hybrid arrangement of a battery-like (as anode) and supercapacitor-like electrodes (as cathode) in organic electrolyte, heading to enhance energy and power densities.[5-7] It has been hyped that LIC bridges the low energy density supercapacitors (SCs) and low power Li-ion batteries (LIBs).[8-9] This good performance of LIC in terms of energy and power density is owed to the coupling effect from the rapid charging rate of capacitor-type electrode, the large specific capacity of the battery-like electrode, and the much wider working potential window of the organic electrolytes.[5, 6] So far, several hybrid LIC designs have been realized, which are based on an activated carbon (AC) cathode combined with graphite, $Li_4Ti_5O_{12}$, vanadates (Li_3VO_4, $BiVO_4$ etc.) or metal oxides anode.[10-16] However, the poor rate capability of graphite, the relatively high redox potential (~1.5 V, vs. Li/Li^+) of $Li_4Ti_5O_{12}$ (LTO) and the poor electrical conductivity and cycle stability of metal oxides hamper their utilization in high performance LICs. Therefore, it is crucial to explore the novel anode materials with high rate capability, good cycle stability and low redox potential to achieve further improvements for hybrid LICs.

Recently, two-dimensional (2D) porous materials have been successfully applied in newly developed energy storage systems due to their large surface area for reaction and interfacial transport, and short diffusion paths.[17-19] Especially, inorganic-organic hybrid porous materials such as metal-organic frameworks (MOFs) with high specific surface area and low density have been claimed to be promising electrode materials for next-generation LIBs and supercapacitors.[19-22] MOFs are building blocks of low cost and cheap metal salts/organic ligands in appropriate solvents.[23] The metal sites can be ions of transition metals, alkaline earth metals, or lanthanides and

organic linkers are typically multidentate molecules with N- or O donor atoms (pyridyl, polyamines, carboxylates, and so on).

Several MOFs have been investigated as promising anode materials for LIBs, where metal cations in MOFs act as active sites for redox reactions, and open crystal frameworks support effective and reversible insertion/extraction for Li ions.[24, 25] However, the chemical stability of MOFs suffers from more severe challenges in the complex electrochemical environment of LIBs. Therefore, the thermal, chemical, and structural stabilities of MOFs are in high demand, which are critical to the cycling performance of LIBs in practical applications. In addition, the electrical conductivity of MOFs is important to the practical specific capacity and rate performance. Thus, MOFs with high electrical conductivity and stability are desirable anode materials for LIBs and LICs. An emerging method to engineer high conductivity anode with good electrochemical performance is to develop porous transition metal oxides embedded in porous carbon matrices using MOFs as sacrificial framework precursors. [27-29] For instance, Li et al. [28] prepared micro-cuboid-like carbon-decorated iron oxide (C-Fe_3O_4) from Fe-MOFs precursors and reported a high reversible capacity of 975 mAh/g over 50 cycles at 100 mA/g. Yang et al. [29] reported ZnO quantum dots@hierarchically porous carbon with high specific capacity of approximately 1200 mAh/g and good cycling stability. However, best of our knowledge there is no report on the utilization of MOF-derived transition metal oxide anode for LICs.

Herein, we engineered hybrid manganese oxide nanoparticles embedded porous graphene-like carbon nanosheets (MnO_2@C-NS) as a promising anode material for lithium ion hybrid capacitor (LIHC) by direct carbonization of a three-dimensional manganese-based MOF $[Mn(1,4\text{-napdc})]_n$ composed with Mn(II) metal ion, 1,4-ndc (ndc= naphthalene dicarboxylate) (Scheme S1).[30] In this hybrid, graphene-like carbon nanosheets can acts as "flexible confinement" to enwrap MnO_2 particles, which can compensate for the volume change of MnO_2 and prevent the detachment and agglomeration of pulverized MnO_2, thus extending the cycling life of the electrode. Moreover, lithium-ion hybrid capacitor (LIHC) fabricated with MnO_2@C-NS as the anode and MOF-derived

nanoporous carbon sheets (prepared from other potassium-based metal-organic framework, NPCS) as cathode yields a working potential of 4.0 V and high values of specific energy and power density as well as long cycle life. This study reveals that MOF based materials can be promising anode and cathode materials for highly efficient and robust LIHC or LIBs.

Results and Discussion

Here we have used a $[Mn(1,4\text{-napdc})]_n$ (1) for preparing a composite of MnO_2 nanoparticle and graphitic carbon support under particular pyrolytic conditions, the detailed experimental procedure is provided in supporting information and scheme S1. The structural integrity of as-synthesized MOF was confirmed by PXRD (Figure S1). In this process, $[Mn(1,4\text{-napdc})]_n$ (1) acts as both sacrificial carbon matrix and manganese precursor. The resulting hybrid material was further characterized by using Raman and XRD techniques to investigate its compositional and structural properties. Raman spectrum of MnO_2@C-NS hybrid (Figure 1a) shows a significant band around 647 cm^{-1}, which might correspond to MnO_2 [31]. A slight displacement in MnO_2 band position compared to literature value might be attributed to the interaction of Mn-O with the carbon matrix. Moreover, two additional bands can be seen at around 1340 and 1593 cm^{-1}, where the former could be assigned to sp^3 carbon and the later to graphitic (sp^2) carbon. In addition, relative intensities of these two bands indicate the dominance of sp^3 carbon over sp^2 carbon, which might be due to the small defects with graphitic carbon environment include bonding disorders and oxygen functional groups. Figure 1 (b) shows the XRD pattern of MnO_2@C-NS, where all the peaks are assigned to the β-MnO_2 phase (JCPDS: 24-0735). No other impurities were found. The composition of the MnO2@C-NS hybrid was further analyzed by XPS (Figure S3a). The deconvoluted high-resolution C1s signal allows the quantitative assignment of two different kinds of carbon atoms. The main peak at 284.7 eV originates from the sp^2 graphitic nature carbon (C–C sp^2) and other peak at 289.34 eV indicates the presence of C=O (Figure 1c). Moreover, core-level Mn3s spectrum exhibits two major peaks at binding energies

of 89.75 and 84.95 eV with a spin-energy separation of 4.8 eV, indicate the presence of tetravalent Mn species in good agreement with literature reports (Figure 1d).[32]

Field-emission scanning electron microscopy (FE-SEM) and transmission electron microscopy (TEM) studies provided insights into morphological and detailed structural characteristics of MnO_2@C-NS (Figure S4). The panoramic view with SEM images from different cross-sections MnO_2@C-NS sample are presented in Figure 2 (a-c), suggesting the formation of layer-by-layer structure consisting of graphene-like carbon nanosheets decorated with MnO_2 nanoparticles. The TEM image (Figure 2d) reveals that these MnO_2 nanoparticles are homogeneously and tightly attached to the graphene-like carbons sheets, even after the ultrasonication used to disperse the MnO_2@C-NS hybrid for TEM characterization. It is further clearly seen from Figure 2 (c-e) that carbon nanosheets wrap MnO_2 nanoparticles, which helps to prevent MnO_2 from agglomeration and enables a good dispersion of these oxide particles over the carbon support. The high-resolution TEM image in Figure 2e shows the interfacial structure between graphene-like carbon nanosheets and the MnO_2 nanoparticles. The well-resolved lattice fringes with an interplanar distance of 0.31 nm is associated to (110) plane of MnO_2. Energy-dispersive X-ray spectroscopy elemental mapping was used to investigate the distribution of MnO_2 particles in the hybrid structure (Figure 2 g, h). It is revealed the uniform dispersion of the MnO_2 particles in the layered structure consisting of graphene-like carbon/MnO_2 hybrid sheets. It is further interesting to note that the MnO_2@CNS hybrid exhibited the BET and Langmuir surface areas of 45 m^2/g and 65 m^2/g, respectively with a large pore volume of 1.09 cm^3/g (Figure S3b). The unique architecture of the interlayered carbon nanosheets anchored MnO_2 nanoparticles possesses a certain amount of macropores and mesopores that form an open porous system, and a limited amount of micropores and small mesopores, which facilitate electrolyte ion diffusion to active sites with less resistance and tolerate the volume change.[33]

The exceptional architecture of MnO_2 nanocrystals incorporated ultrathin carbon nanosheets (MnO_2@C-NS) makes it promise for energy storage applications. Therefore, the electrochemical

performance of the MnO_2@C-NS was investigated as an anode material for LIB. Figure 3 (a) displays initial few CV curves for MnO_2@C-NS anode in a potential window of 0.01 to 3.0 V at 1 mV s^{-1} scan rate. The first cathodic scan shows a peak around 0.52 V, corresponding to the formation of solid electrolyte interface (SEI) at the electrode surface [34] which disappeared in the next subsequent cycle. The sharp peak observed near 0.10 V suggest the reduction of Mn^{2+} to Mn^0 [35, 36,] which shifts to 0.30 V in the next cycle, indicating an irreversible phase transformation that leads to the formation of metallic manganese and Li_2O. [37] Conversely, in the anodic scan, two peaks at 1.29 V and 2.1 V indicate two-step electrochemical oxidation reaction. The wide oxidation peak at about 1.29 V may be associated to the oxidation of Mn^0 to Mn^{2+} [38] while a very small peak at 2.1 V may be originated from the re-oxidation of Mn(II) to a higher oxidation state promoting from the fast Li reaction kinetics and synergistic effects of carbon and MnOx.[38, 39] From the second cycle, the CV curves tend to overlap, suggesting the excellent cycling stability.

The charge/discharge profiles for MnO_2@C-NS unambiguously support the claims made from CV curves. Figure 3 (b) displays the first ten charge/discharge curves for the MnO_2@C-NS at a current density of 0.1 A g^{-1}. In the first discharge, a small plateau at around 0.53 V and, a slop thereafter to 0.01 V is clearly observed, which may be associated to the SEI formation and the reduction of Mn^{2+} to Mn^0 during Li-insertion, respectively. [40, 41] The initial discharge and charge capacities of the MnO_2@C-NS were found to be 1546 and 985 mAh/g, respectively with initial Coulombic efficiency of 63.7 %. The sudden drop in the initial capacity is attributed to the decomposition of electrolyte and formation of SEI layer, which normally observed in metallic oxide-based anodes. [42-45] Figure 3 (c) shows the rate performance of the MnO_2@C-NS at different current densities. Notably, MnO_2@C-NS nanocomposite delivered excellent reversible capacities of 1054 mAh/g and 323 mAh/g at 0.1 A/g and 20 A/g, respectively. Thus, even at very high current density, the MnO_2@C-NS delivered a reversible capacity of 333 mAh/g, which is still a very substantial value (about 86 % of the theoretical capacity of graphite). Moreover, when the current density changed back to 0.1 A/g after 100 cycles, the MnO_2@C-NS nanocomposite could achieve a capacity of 1021

mAh/g, demonstrating excellent rate capability. The capacity obtained for MnO_2@C-NS nanocomposite is significantly higher than previously reported values (see Table S1), which might be ascribed to the porous structure of MnO_2@C-NS electrode, that offers an easy access to electrolyte ions and generates large number of electroactive sites, resulting in excellent capacity and rate capability.[46, 47]

The Li-ion charge kinetics of MnO_2@C-NS were further characterized by estimating the capacitive and diffusion-controlled charge contributions to the total charges stored in the electrode. [48] Generally, the storage mechanism can be revealed by the dependence of the current (i) on the scan rate (v) [49]:

$$i = a v^b \qquad (1)$$

where a and b are adjustable parameters; b = 0.5 corresponds to the semi-infinite diffusion process, and b = 1 indicates a capacitive process.[50] In this context, the CV curves were recorded at different scan rates (from 1 mV/s to 10 mV/s) for MnO_2@C-NS electrode (Figure S5). There is a good linear relationship between the current and the scan rate with R^2 = 0.9967 and 0.9984 for the cathodic and anodic scans, respectively. In addition, the slope of the corresponding log(v) vs log(i) plot is b = *0.68*, suggesting the kinetics dominated by diffusion-controlled process (Figure S6a). In order to calculate, the capacitive charge contribution to the total current response, Equation (1) can be re-written as,

$$i = k_1 v + k_2 v^{1/2} \qquad (2)$$

Thus, the current at a fixed potential is equal to the sum of capacitive contribution ($k_1 v$) and diffusion-controlled contribution ($k_2 v^{1/2}$).[51] The constants k_1 and k_2 can be determined by plotting $i/v^{1/2}$ versus $v^{1/2}$ and measuring the slope and the y-axis intercept point of a straight line, respectively. As shown in Figure S5, the shaded area ($k_1 v$) with the experimental currents, it is found that about 73 % of the total current of the MnO_2@C-NS electrode is contributed by the diffusion-controlled process at 1 mVs^{-1}. Figure 3 (d) present the percent contribution of separate capacitive and diffusion-controlled charge contributions measured at different scan rates. The Li-ion

diffusion coefficient in MnO_2@C-NS electrode was further estimated by the Randles-Sevick equation [52]

$$i_p = 2.69\times10^5 n^{3/2} A D_{Li}^{1/2} \nu^{1/2} C \qquad (3)$$

where i_p is current maximum in amps (we considered current value at 3 points), n is number of electrons involved in the charge storage, A is electrode area in cm^2 (for simplicity we have considered geometrical area), D_{Li} is diffusion coefficient in cm^2/s, ν is scan rate in V/s, C is concentration of Li-ion in mol/cm^3. The diffusion coefficients for MnO_2@C-NS calculated at different points is in the range of 10^{-9}- 10^{-11} cm^2/s for different scan rates (see Figure S6b). The diffusion coefficients for MnO_2@C-NS increases slowly with scan rate, further confirming the high rate capability of the material. Long-term cycling stability is a key parameter in energy storage systems, which defines the practical suitability of material. The cycling performance of MnO_2@C-NS was investigated at 0.5 A/g over 1000 cycles and presented in Figure 3 (e). It is evidenced that the nanocomposite displayed an excellent cycling stability around 90 % retention over 1000 charge/discharge cycles. Moreover, the Coulombic efficiency of MnO_2@C-NS electrode is remarkably improved after first few charge/discharge cycles and stabilized at around 99 % over 1000 cycles. This long cycling performance may be attributed to the unique nano-architecture of MnO_2@C-NS where MnO_2 nanocrystals are wrapped in the graphene-like carbon nanosheets. In such a nanostructure, graphene-like nanosheets not only provides a conducting scaffold for MnO_2 nanocrystals but also offers ion-buffering reservoir to suppress the volume expansion during charge/discharge cycles while MnO_2 nanocrystals deliver high capacity through their faradic charge storing mechanism. Thus, the synergic combination of MnO_2 nanocrystals and graphene-like carbon nanosheets together offers high capacity with complementary long-term cycling stability.

The extraordinary properties of the MnO_2@C-NS electrode can be attributed to its unique porous MnO_2 nanocrystals wrapped graphene-like carbon nanosheets architecture, which reduces the mass-transfer resistances, and offer high intrinsic conductivity for smoothing electron transport. Thus,

such a high Li-ion storage capacity, excellent rate/cycling stabilities and adequate voltage range of MnO_2@C-NS make it an excellent candidate as anode for hybrid Li-ion capacitors.

The cathode material: MOF derived nanoporous carbon nanosheets (NPCS)

To develop high performance cathode materials in LICs, the key is to engineer high surface area, tunable pore size and high conductivity carbon materials. Herein, we have prepared controlled 2D nanoporous carbon sheets (NPCS) by direct carbonization of a specifically selected two-dimensional potassium-based MOF as described in our previous report. [13] XRD pattern of NPCS shows characteristic (d_{002}) graphitic peak of carbon materials at around at 24.3° while the two intense bands for carbon materials are clearly observed at around 1340 and 1593 cm^{-1} in Raman spectrum (Figure S7). Moreover, Raman analysis suggest the existence of small defects in NPCS with graphitic carbon environment.[53] The TEM image of nanoporous carbon nanosheets (NPCS) (Figure 4 (a)) reveals the existence of ultrathin nanosheets with a layered structure. The BET surface area was determined to be 1292 m^2g^{-1} with a large pore volume of 1.06 cm^3g^{-1} that can provide a short ion-transport pathway with a minimized inner-pore resistance. The resulting layered 2D carbon nanostructure provides excellent specific surface area and pore volume that can significantly enhance the charges stored at the electrode surface.

The NPCS cathode was initially tested in a Li half-cell between 1.5-4.5 V vs. Li/Li^+ and the results are displayed in Figure 4 (b-e). The nearly rectangular CV curves with small humps are observed for NPCS cathode at all the scan rates, indicating major contribution from EDLC with small contribution from pseudo-capacitance due to surface oxygen groups (Figure 4b). Moreover, the linear relationship between current density and scan rates in CV curves confirmed that the electrochemical reactions in the NPCS cathode were not diffusion-limited but confined to the surface.[54] The galvanostatic charge-discharge (GCD) curves of NPCS at different current densities from 0.1 A/g to 15.6 A/g are presented in Figure S8. The GDC profiles show linear and symmetric nature without any plateau and distinct inflection points, confirming the capacitive charge storage behavior of NPCS electrode. The first discharge capacity of NPCS was 133 mAh/g at a current

density of 0.1 A/g (Figure 4c), which is comparable to a previously reported cathode [55-57]. The rate capability test suggested remarkably fast Li storage capability in the NPCS cathode (Figure 4d). Even at high current rate of 15.6 A/g, the NPCS showed a specific capacity of 56.7 mAh/g (42 % of initial capacity) and the initial capacity was recovered when the current rate was returned to 0.1 A/g, indicating excellent reversibility. It is further interesting to note that, the NPCS cathode exhibits excellent cycling stability with 86 % capacity retention over 7000 cycles at current density of 2.4 A/g (see Figure 4 (e)). Upon repeated cycles, the high specific capacity was maintained with a Coulombic efficiency of 100 %. Thanks to the unique ultrathin graphene-like layered structure of NPCS, which offers high surface area and adequate pore volume for high charge storage capabilities (large Li^+ uptake) and long cycling stability.

Considering all these excellent electrochemical properties of NPCS in $LiPF_6$ electrolyte and its complementary electrochemical voltage, NPCS was expected to be a suitable cathode electrode to be paired with MnO_2@C-NS anode in a LIC.

Li-ion hybrid capacitor (LIHC) based on MnO_2@C-NS anode and NPCS cathode

Although recent advancements in the development of Li-ion capacitors (LICs) using Li-intercalated materials (e.g. $LiCoO_2$) and activated carbon (AC) electrodes, they still may have some significant drawbacks. [5, 6] For example, it is very difficult to fully utilize the overall specific energy density of such battery electrodes due to the redox reaction kinetics being too slow in LIC systems. This inherent difference can diminish the energy storage ability of the electrochemical device especially during fast charge-discharge processes compromising their practical applications. This drawback requires the design of advanced electrodes, which could help offsetting the low charge-transfer kinetics intrinsic to redox reactions of battery electrodes. In this context, our MnO_2 nanocrystals wrapped graphene-like carbon nanosheets (MnO_2@C-NS) would be promising hybrid anode for LIHC where MnO_2 nanocrystals reduces the diffusion path of charge-compensating ions and graphene-like carbon nanosheets provide extra electronic conductivity. In addition, it also provides

the opportunity to get all-in-one faradaic and capacitive activities displayed in parallel, which might further helps to lessen the kinetic mismatch problem associated to LIHCs.

Herein, we have fabricated LIHC full cell using MnO_2@C-NS as anode and highly porous NPCS as cathode material by taking advantage of their different working potential windows as shown in Figure 3a and 4b. Note that, the masses of the cathode and anode must be adjusted to match the capacity, due to the specific capacity difference between MnO_2@C-NS and NPCS electrodes. We thus used an optimized mass ratio of 1:7.6 between the MnO_2@C-NS and NPCS electrode.

of specific capacitance and capacity with current density for MnO_2@C-NS//NPCS cell.

Thus, we have provided double hybridization approach, that is, the simultaneous combination of faradaic and capacitive materials in a single electrode (MnO_2@C-NS) and their use in front of a capacitive one (NPCS). In effect, this strategy would be equivalent to a combination of faradaic and capacitive materials in parallel AND in series, thus improving kinetic aspects as well as larger voltages and energy densities. The reaction kinetics of LIHC is presented in Figure 5 (a) where Li ions rapidly transferred/extracted into/from MnO_2@C-NS through surface faradic reactions, while PF^{6-} anions swiftly adsorbed/desorbed on the porous NPCS cathode during charge/discharge processes, respectively. The electrochemical performances of MnO_2@C-NS//NPCS LIHC cell was tested within the voltage range of 0.01-4.0 V. In order to understand the charge storage mechanism, the charge/discharge curves of MnO_2@C-NS//NPCS cell were recorded at 0.5 A/g with corresponding potential profiles of cathode (black) and anode (red) with respect to Li-metal (see Figure 5 (b)). As expected, the anode and cathode electrodes work in the potential ranges: 0.01 V to 2.0 V and 2.0 V to 4.0 V (vs Li/Li^+), respectively. In MnO_2@C-NS hybrid electrode, the graphene-like carbon nanosheets first charged by electrostatic forces in the initial state (Figure 5b, Region I) until the electrode potential reaches the redox reaction potential of the MnO_2 nanocrystals. Then MnO_2 nanocrystals charged through the redox reactions while maintaining the potential of the hybrid electrode, until the faradaic component (MnO_2) reaches its full-charge state (Region II) as seen in Figure 5 (b). After the full charge of the MnO_2, the carbon nanosheets is charged again

(Region III) until the maximum potential of the hybrid electrode is reached. Thus, the total amount of energy stored in MnO_2@C-NS hybrid system is the sum of energy stored in the MnO_2 nanocrystals and carbon nanosheets. The hybrid electrode is bound to have improved power densities due to the carbon nanosheets, which can also store electrochemical energy by electrostatic force, enhances the electron transfer to the MnO_2 nanocrystals in the hybrid electrode system, causing a better charge transfer reaction at high rates. Figure 5 (c) shows GCD curves for LIHC cell at different current densities from 0.45 A/g to 2.91 A/g. The shapes of GCD curves at different current densities exhibit quasi-symmetric triangular-shape, suggesting good combination between the hybrid MnO_2@C-NS anode and EDLC NPCS cathode. Interestingly, it is further evidenced that the LIHC cell provide low IR drop, suggesting good electrical conductivity of the materials. The variations of specific capacitance and specific capacity with current densities are shown in Figure 5 (d). The capacity of the full LIHC cell was calculated to be 129 mAh/g, considering total weight of active materials in both electrodes (mass of active materials in cathode and anode).

A Ragone plot is the graphical representation of the balance between energy and power density, which is key for many practical applications. The energy and power density values of MnO_2@C-NS//NPCS LIC cell at different current densities were calculated from the GCD curves and presented in Figure 6 (a). The device is able to achieve a maximum energy density of 166 Wh/kg (at a power density of 550 W/kg) and a maximum power density of 3.9 kW/kg (at energy density of 49.3 Wh/kg). The integrated performance (energy density *vs.* power density) is best compared with most reported LICs such as MnO-C//CNS, $Li_4Ti_5O_{12}$//TRGO, HC//AC, LTO//AC, C-LTO//AC etc. [7, 13, 57-70 and Table S2]. More remarkably, from Figure 6 (b), the LIHC exhibits superior long-term cycling stability with ~91% capacity retention after 5000 cycles at 1 A/g as well as excellent Coulombic efficiency (nearly 98% retained after the cycling test). The initial increase in the capacity might be attributed to the activation of MnO_2@C-NS electrode.

We have designed an advanced MOF derived MnO_2 nanocrystals wrapped graphene-like carbon nanosheets (MnO_2@C-NS) hybrid anode and nanoporous carbon sheets (NPCS) cathode for

high performance LIC, which can surpass the main intrinsic drawbacks of kinetics and capacity mismatch in such a combined system. Such a high performance of MnO_2@C-NS//NPCS LIC might be ascribed to the following characteristics (Figure 6c): 1) the porosity between graphene-like nanosheets in MnO_2@C-NS anode facilitates Li ion transport, which offer high capacity and excellent rate capability. 2) the interleaved structure of graphene-like nanosheets homogeneously confine the MnO_2 nanoparticles that inhibits the volume change, alleviating the stress of MnO_2 particles, and preventing the detachment and agglomeration of pulverized MnO_2 during cycling. 3) the MOF derived nanoporous carbon nanosheets (NPCS) provides a conductive network, high surface area, short diffusion lengths which are optimal for adsorption/desorption of electrolyte ions, thereby providing both improved energy and power densities.

Conclusions

In conclusion, a novel Li-ion hybrid capacitor (LIHC), combining MOF-derived MnO_2 nanoparticles decorated graphene-like carbon nanosheets (MnO_2@C-NS) anode and ultrathin nanoporous carbon nanosheets (NPCS) cathode, is successfully designed and investigated for the first time. The MnO_2@C-NS//NPCS hybrid device exhibits energy densities of 166-49 Wh/kg over the power densities from 550 to 3.5 kW/kg, which are considerably higher than the previous reports. The high-performance of the hybrid system is attributed to both MOF derived graphene-like carbon nanosheets-enhanced electrode materials. As-prepared MnO_2@C-NS anode achieves both high specific capacity of 1054 mAh/g at 0.1 A/g and good rate performance with good cycle stability (90% over 1000 cycles); meanwhile, the cathode electrode material ultrathin nanoporous carbon sheets (NPCS) shows high EDLC specific capacitance as well as rate capability with excellent stability (86% over 7000 cycles). These combined features make the hybrid supercapacitor exhibit a remarkable energy density much higher than the commercial supercapacitors and can even compare with commercial lithium-ion batteries with improved power density.

Supporting Information

Supporting Information is available from the Wiley Online Library or from the author.

Acknowledgements

K.J. and D.P.D. contributed equally to this work. K.J. is grateful to the Alexander von Humboldt (AvH) foundation for a postdoctoral fellowship. D.P.D. acknowledges the support of University of Adelaide, Australia for grant of Research Fellowship (VC Fellow). The authors also gratefully acknowledge support by the Catalysis Research Centre at TU Munich and the support from the Ministry of Education, Youth and Sports of the Czech Republic (LO1305) and the assistance provided by the Research Infrastructure NanoEnviCz, supported by the Ministry of Education, Youth and Sports of the Czech Republic under Project No. LM2015073. The authors also gratefully acknowledge support by the Catalysis Research Centre at TU Munich and the support by the Operational Programme Research, Development and Education—European Regional Development Fund, projects no. CZ.02.1.01/0.0/0.0/15_003/0000416 and CZ.02.1.01/0.0/0.0/16_019/0000754 of the Ministry of Education, Youth and Sports of the Czech Republic. M.P. acknowledges the internal project IGA_PrF_2018_015 of Palacký University in Olomouc.

Received: ((will be filled in by the editorial staff))
Revised: ((will be filled in by the editorial staff))
Published online: ((will be filled in by the editorial staff))

References

[1] D. P. Dubal, O. Ayyad, V. Ruiz, P. Gomez-Romero, *Chem. Soc. Rev.* **2015**, *44*, 1777.

[2] M. Salanne, B. Rotenberg, K. Naoi, K. Kaneko, P. -L. Taberna, C. P. Grey, B. Dunn, P. Simon, *Nat. Energy* 2016, 1, 16070.

[3] K. Naoi, W. Naoi, S. Aoyagi, J. Miyamoto, T. Kamino, *Acc. Chem. Res.* **2013**, *46*, 1075

[4] D. P. Dubal, N. R. Chodankar, D. H. Kim, P. Gomez-Romero, *Chem. Soc. Rev.* **2018,** *47*, 2065

[5] K. Naoi, S. Ishimoto, J. Miyamoto, W. Naoi, *Energy Environ. Sci.* **2012**, 5, 9363.

[6] V. Aravindan, J. Gnanaraj, Y.S. Lee, S. Madhavi, *Chem. Rev.* **2014**, *114*, 11619.

[7] D. P. Dubal, P. Gomez-Romero, *Mater. Today Energy* **2018**, *8*, 109.

[8] F. Zhang, T. Zhang, X. Yang, L. Zhang, K. Leng, Y. Huang, Y. Chen, *Energy Environ. Sci.* **2013**, *6*, 1623

[9] R. Wang, P. Liu, J. Lang, L. Zhang, X. B. Yan, Energy Storage Materials,

2017, *6*, 53.

[10] V. Khomenko, E. Raymundo-Piñero, F. Béguin, *J. Power Sources* **2008**, *177*, 643.

[11] K. Leng, F. Zhang, L. Zhang, T. Zhang, Y. Wu, Y. Lu, Y. Huang, Y. Chen, *Nano Res.* **2013**, *6*, 581.

[12] E. Iwama, N. Kawabata, N. Nishio, K. Kisu, J. Miyamoto, W. Naoi, P. Rozier, P. Simon, K. Naoi, *ACS Nano*, **2016**, *10*, 5398

[13] D. P. Dubal, K. Jayaramulu, R. Zboril, R. A. Fischer, P. Gomez-Romero, *J. Mater. Chem. A*, **2018**, *6*, 6096

[14] M. Yang, Y. Zhong, J. Ren, X. Zhou , J. Wei, Z. Zhou, *Adv. Energy Mater.* **2015**, *5*, 1500550.

[15] H. Wang, Z. Xu, Z. Li, K. Cui, J. Ding, A. Kohandehghan, X. Tan, B. Zahiri, B. C. Olsen, C. M. B. Holt, D. Mitlin, *Nano Lett.* **2014**, *14*, 1987.

[16] L. Kong, C. Zhang, J. Wang, W. Qiao, L. Ling, D. Long, *ACS Nano* **2015**, *9*, 11200.

[17] A. Vlad, A. Balducci, *Nat. Mater.* **2017**, *16*, 161

[18] Y. Li, Z. Y. Fu, B. L. Su, *Adv. Funct Mater.* **2012**, *22*, 4634.

[19] K. Jayaramulu, D. P. Dubal, B. Nagar, V. Ranc, O. Tomanec, M. Petr, R. Datta, R. Zboril, P. Gómez- Romero, A. Fischer Roland, *Adv. Mater.* **2018**, *30*, 1705789

[20] G. Xu, P. Nie, H. Dou, B. Ding, L. Li, X. Zhang, *Mater. Today*, **2017**, *20*, 191-209

[21] H. Wang, Q. L. Zhu, R. Zou, Q. Xu, *Chem* **2017**, *2*, 52-80.

[22] P. Pachfule, D. Shinde, M. Majumder and Q. Xu, *Nat Chem*, **2016**, ***8***, 718-724

[23] S. Dissegna, K. Epp, R. Heinz Werner, G. Kieslich, A. Fischer Roland, *Adv. Mater.* **2018**, 1704501

[24] J. B. Goodenough, Y. Kim, *Chem. Mater.* **2010**, *22*, 587.

[25] B. M. Wiers, M. L. Foo, N. P. Balsara, J. R. Long, *J. Am. Chem. Soc.* **2011**, *133*, 14522.

[27] L. Hou, L. Lian, L. Zhang, G. Pang, C. Yuan, X. Zhang, *Adv. Funct. Mater.* **2015**, *25*, 238.

[28] M. Li, W. Wang, M. Yang, F. Lv, L. Cao, Y. Tang, R. Sun, Z. Lu, *RSC Adv.* **2015**, *5*, 356.

[29] S. J. Yang, S. Nam, T. Kim, J. H. Im, H. Jung, J. H. Kang, S. Wi, B. Park, C. R. Park, *J. Am. Chem. Soc.* 2013, 135, 7394-7397.

[30] T. K. Maji, W. Kaneko, M. Ohba, S. Kitagawa, *Chem. Commun.* **2005**, 0, 4613-4615

[31] S. Yu, R. Liu, W. Yang, K. Han, Z. Wang, H. Zhu, *J. Mater. Chem. A*, **2014**, 2, 5371

[32] D. P. Dubal, D. Aradilla, G. Bidan, P. Gentile, T. J. S. Schubert, J. Wimberg, S. Sadki, P. Gomez-Romero, *Sci. Rep.* **2015**, *5*, 09771

[33] S. B. Yang, G. L. Cui, S. P. Pang, Q. Cao, U. Kolb, X. L. Feng, J. Maier, K. Mullen, *ChemSusChem*, **2010**, *3*, 236.

[34] B. Sun, Z. Chen, H. S. Kim, H. Ahn, G. Wang, *J. Power Sources* **2011**, *196*, 3346.

[35] K. Zhang, P. Han, L. Gu, L. Zhang, Z. Liu, Q. Kong, C. Zhang, S. Dong, Z. Zhang, J. Yao, H. Xu, G. Cui, L. Chen, *ACS Appl. Mater. Interfaces* **2012**, *4*, 658.

[36] Y. Xiao, X. Wang, W. Wang, D. Zhao, M. Cao, *ACS Appl. Mater. Interfaces* **2014**, *6*, 2051

[37] H. Jiang, Y. Hu, S. Guo, C. Yan, P. S. Lee, C. Li, *ACS Nano* **2014**, *8*, 6038.

[38] G. Zhao, X. Huang, X. Wang, P. Connor, J. Li, S. Zhang, J. T. S. Irvine, *J. Mater. Chem. A* **2015**, *3*, 297.

[39] Y. J. Mai, D. Zhang, Y. Q. Qiao, C. D. Gu, X. L. Wang, J. P. Tu, *J. Power Sources* **2012**, *216*, 201.

[40] S. B. Wang, Y. L. Xing, X. Liu, H. Z. Xu, S. C. Zhang, *RSC Adv.* **2016**, *6*, 79066.

[41] B. L. Liu, D. Li, Z.J. liu, L.L. Gu, W. H. Xie, Q. Li, P. Q. Guo, D.Q. Liu, D. Y. He, *Appl. Surf. Sci.* **2017**, *394*, 1.

[42] F. C. Zheng, M. N. He, Y. Yang, Q. W. Chen, *Nanoscale* **2015**, *7*, 3410.

[43] F. C. Zheng, D. Q. Zhu, X. H. Shi, Q. W. Chen, *J. Mater. Chem. A* **2015**, *3*, 2815.

[44] X. L. Jia, Z. Chen, X. Cui, Y. T. Peng, X. L. Wang, G. Wang, F. Wei, Y. F. Lu, *ACS Nano* **2012**, *6*, 9911.

[45] D. Sun, Y. G. Tang, D. L. Ye, J. Yan, H. S. Zhou, H. Y. Wang, *ACS Appl. Mater. Interface* **2017**, *9*, 5254.

[46] S. Z. Haung, Y. Cai, J. Jin, J. Liu, Y. Li, Y. Yu, H. E. Wang, L. H. Chen, B. L. Su, *Nano Energy* **2015**, *12*, 833.

[47] S. Z. Haung, Y. Cai, J. Jin, J. Liu, Y. Li, H. E. Wang, L. H. Chen, T. Hasan, B. L. Su, *J. Mater. Chem. A* **2016**, *4*, 4264.

[48] Z. Chen, V. Augustyn, X. Jia, Q. Xiao, B. Dunn, Y. Lu, *ACS Nano* **2012**, *6*, 4319.

[49] M. Sathiya, A. S. Prakash, K. Ramesha, J. M. Tarascon, A. K. Shukla, *J. Am. Chem. Soc.* **2011**, *133*, 16291

[50] P. Simon, Y. Gogotsi, B. Dunn, *Science* **2014**, *343*, 1210.

[51] J. Wang, J. Polleux, J. Lim, B. Dunn, *J. Phys. Chem. C* **2007**, *111*, 14925.

[52] L. L. Zhou, S. Y. Shen, X. Peng, L. N. Wu, Q. Wang, C. H. Shen, T. T. Tu, L. Huang, J. T. Li, S. G. Sun, *ACS Appl. Mater. Interfaces*, **2016**, *8*, 23739

[53] Y. Liang, J. Wei, Y. X. Hu, X. F. Chen, J. Zhang, X. Y. Zhang, S. P. Jiang, S. W. Tao, H. T. Wang, *Nanoscale* **2017**, *9*, 5323.

[54] S. W. Lee, N. Yabuuchi, B. M. Gallant, S. Chen, B. S. Kim, P. T. Hammond, Y. S. Horn, *Nat. Nanotechnol.* **2010**, *5*, 531.

[55] Q. Wang, Z. Wen, J. Li, *Adv. Funct. Mater.* **2006**, 16, 2141

[56] A. Banerjee, K.K. Upadhyay, D. Puthusseri, V. Aravindan, S. Madhavi, S. Ogale, *Nanoscale* **2014**, *6*, 4387.

[57] V. Aravindan, D. Mhamane, W.C. Ling, S. Ogale, S. Madhavi, *ChemSusChem* **2013**, *6*, 2240.

[58] Y. Zhao, Y. Cui, J. Shi, W. Liu, Z. Shi, S. Chen, X. Wang, H. Wang, *J. Mater. Chem. A*, **2017**, *5*, 15243

[59] H. Wang, Z. Xu, Z. Li, K. Cui, J. Ding, A. Kohandehghan, X. Tan, B. Zahiri, B. C. Olsen, C. M. Holt and D. Mitlin, *Nano Lett.*, **2014**, *14*, 1987-1994.

[60] W. J. Cao and J. P. Zheng, *J. Power Sources*, **2012**, *213*, 180

[61] H. Wang, Y. Zhang, H. Ang, Y. Zhang, H. T. Tan, Y. Zhang, Y. Guo, J. B. Franklin, X. L. Wu, M. Srinivasan, H. J. Fan and Q. Yan, *Adv. Funct. Mater.*, **2016**, *26*, 3082

[62] H. S. Choi, J. H. Im, T. Kim, J. H. Park and C. R. Park, *J. Mater. Chem.* **2012**, *22*, 16986-18993

[63] Y. Cai, B. Zhao, J. Wang and Z. Shao, *J. Power Sources*, **2014**, *253*, 80-89.

[64] A. Jain, V. Aravindan, S. Jayaraman, P. S. Kumar, R. Balasubramanian, S. Ramakrishna, M. Srinivasan, M. P. Srinivasan, *Sci. Rep.* **2013**, *3*, 3002

[65] H. Y. Wei, D. S. Tsai, C. L. Hsieh, *RSC Adv.*, **2015**, *5*, 69176

[66] F. Zhang, T. Zhang, X. Yang, L. Zhang, K. Leng, Y. Huang, Y. Chen, *Energy Environ. Sci.*, **2013**, *6*, 1623.

[67] R. Wang, J. Lang, P. Zhang, Z. Lin, X. Yan, *Adv. Funct. Mater.* **2015**, *25*, 2270

[68] Z. Chen, V. Augustyn, J. Wen, Y. Zhang, M. Shen, B. Dunn, Y. Lu, *Adv. Mater.* **2011**, *23*, 791.

[69] Q. Wang, Z. Wen, J. Li, *Adv. Funct. Mater.* **2006**, *16*, 2141

[70] V. Aravindan, M. V. Reddy, S. Madhavi, S. G. Mhaisalkar, G. V. Subba Rao, B. V. R. Chowdari, *J. Power Sources* **2011**, *196*, 8850.
T. K. Maji, W. Kaneko, M. Ohba, S. Kitagawa, *Chem. Commun.* **2005**, 4613-4615.

Figure captions

Figure 1 (a and b) Raman spectrum and XRD pattern for **MnO_2@C-NS** nanocomposite, respectively (c, d) Core-level XPS spectra of C1s (C1s spectrum is deconvoluted in three small peaks) and Mn3s for MnO_2@C-NS nanocomposite, respectively.

Figure 2 (a-c) FESEM image of **MnO_2@C-NS** nanocomposite at different magnifications, suggesting formation of interleaved architecture. (d-e) TEM and HRTEM images of MnO_2@C-NS nanocomposite, respectively, suggesting decoration of MnO_2 nanoparticles on graphene-like carbon nanosheets (f) STEM image of **MnO_2@C-NS** nanocomposite. (g-h) EDAX mapping of MnO_2@C-NS nanocomposite with corresponding EDS spectrum, confirming the presence of Mn, O and C without any impurities.

Figure 3 Electrochemical properties of MnO_2@C-NS nanocomposite in Li-half cell configuration: (a) First few cyclic voltammetry curves recorded at scan rate of 1 mV/s. (b) Initial ten galvanostatic charge/discharge curves measured at 0.1 A/g. (c) Variation of specific capacity with cycling at different current rates. (d) Plot of capacitive charge contribution to total charge at different scan rates, (d) Cycling stability and Coulombic efficiency at 0.5 A/g, showing capacity retention of 90 % after 1000 cycles.

Figure 4 (a) HRTEM image of NPCS, showing highly porous, ultrathin interconnected nanosheets network. (b-c) Electrochemical properties of MOF derived nanoporous carbon nanosheets (NPCS) electrode in a Li half-cell within the potential range of 1.5 to 4.5 V (vs Li/Li^+). (b) Cyclic voltammetry curves at different scanning rates. (c) Galvanostatic charge/discharge curves at current density of 0.1 A/g, (d) Rate capability properties of NPCS at different current densities, (d) Long-term cycling stability measured over 7000 cycles at 2.4 A/g.

Figure 5 Electrochemical properties of MnO_2@C-NS//NPCS LIHC full cell in voltage range of 0.01 to 4 V: (a) schematic illustration of design of unique LIHC. (b) CD curve for MnO_2@C-NS//NPCS LIHC cell at current density of 0.5 A/g with corresponding potential distribution across MnO_2@C-NS anode and NPCS cathode versus Li-foil reference electrode. (c) GCD curves for MnO_2@C-NS//NPCS LIHC cell at different current densities, (d) Variation of specific capacitance and capacity with current density for MnO_2@C-NS//NPCS cell.

Figure 6 (a) Ragone plot for MnO_2@C-NS//NPCS LIC device with comparison of previously reported. (b) Capacity retention and Coulombic efficiency of MnO_2@C-NS//NPCS LIHC cell over 5000 cycles, suggesting excellent cycling stability with >98 % Coulombic efficiency. (c) Schematic presentation of charge storing mechanism in MnO_2@C-NS hybrid electrode.

Figure 1

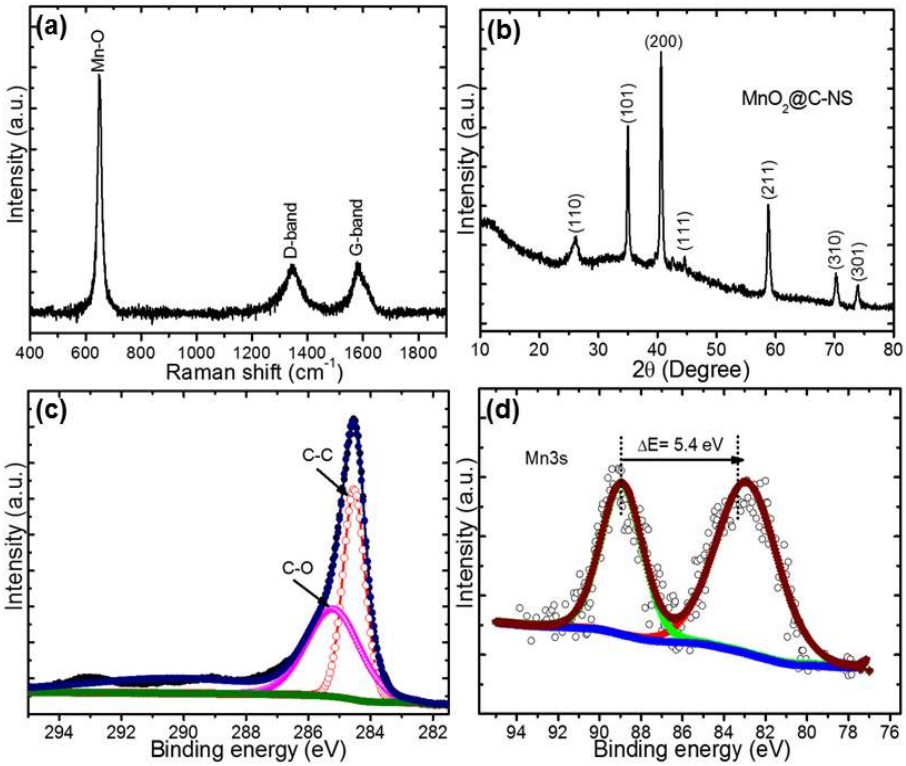
(a)
Mn-O
D-band
G-band
Intensity (a.u.)
Raman shift (cm-1)
(b)
(200)
(101)
MnO2@C-NS
(110)
(111)
(211)
(310)
(301)
Intensity (a.u.)
2θ (Degree)
(c)
C-C
C-O
Intensity (a.u.)
Binding energy (eV)
(d)
Mn3s
ΔE= 5.4 eV
Intensity (a.u.)
Binding energy (eV)

Figure 2

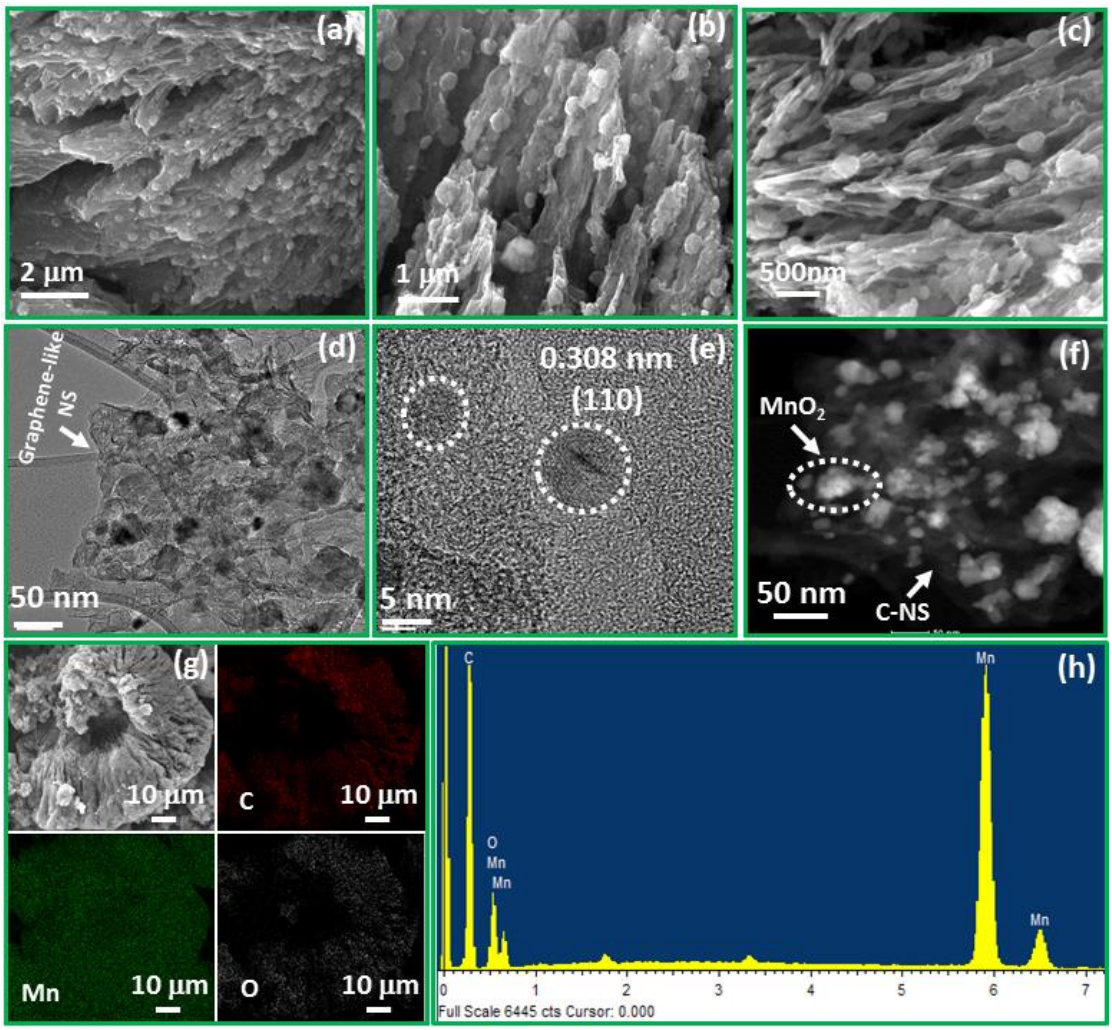
(a)
2 µm
(b)
1 µm
(c)
500nm
(d)
Graphene-like NS
50 nm
(e)
0.308 nm
(110)
5 nm
(f)
MnO2
50 nm
C-NS
(g)
10 µm
C
10 µm
Mn
10 µm
O
10 µm
(h)
C
O
Mn
Mn
Mn
Mn
0
1
2
3
4
5
6
7
Full Scale 6445 cts Cursor: 0.000

Figure 3

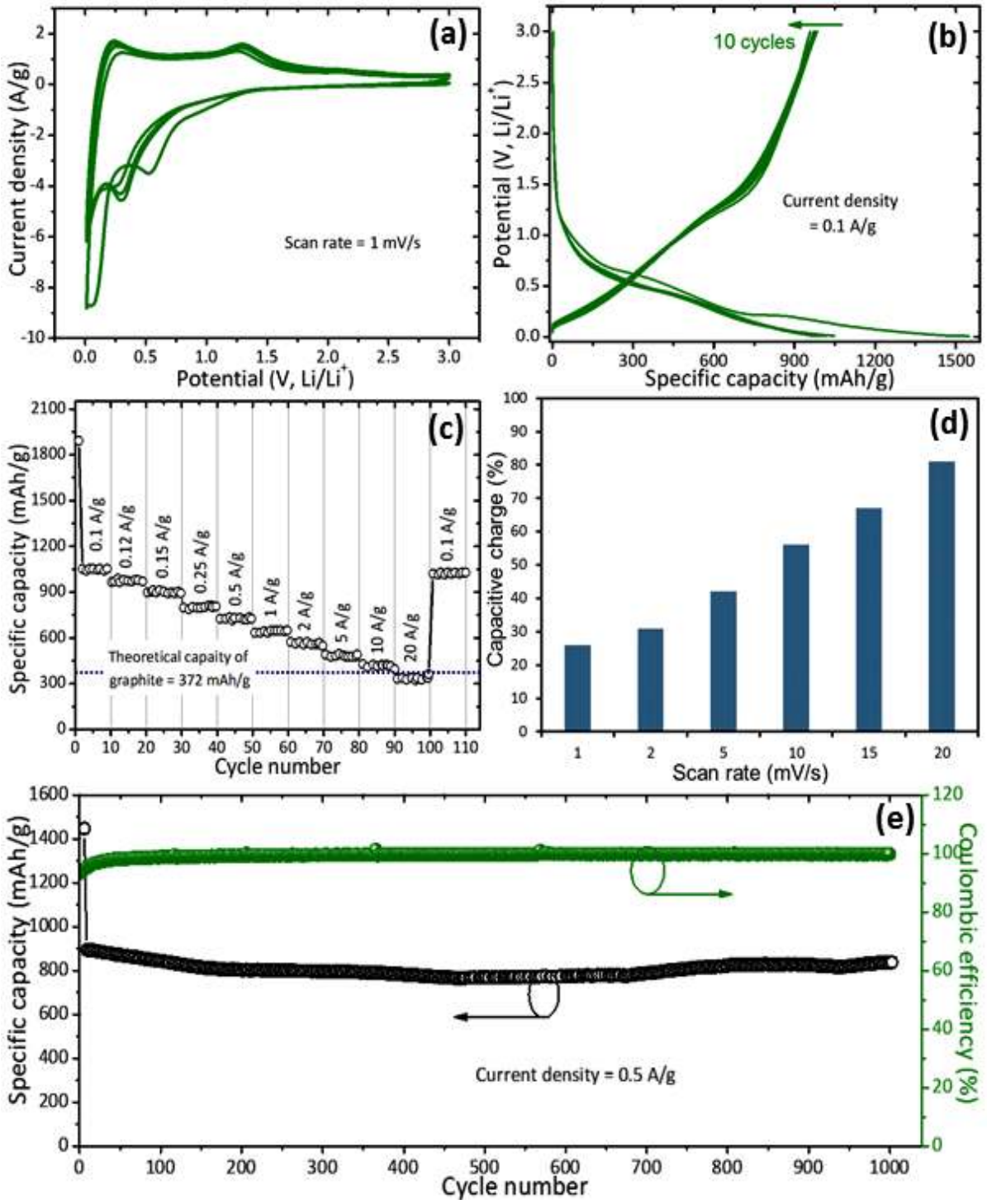
(a)
Current density (A/g)
Potential (V, Li/Li+)
Scan rate = 1 mV/s
(b)
10 cycles
Potential (V, Li/Li+)
Specific capacity (mAh/g)
Current density
= 0.1 A/g
(c)
Specific capacity (mAh/g)
Cycle number
0.1 A/g
0.12 A/g
0.15 A/g
0.25 A/g
0.5 A/g
1 A/g
2 A/g
5 A/g
10 A/g
20 A/g
0.1 A/g
Theoretical capaity of
graphite = 372 mAh/g
(d)
Capacitive charge (%)
Scan rate (mV/s)
(e)
Specific capacity (mAh/g)
Coulombic efficiency (%)
Cycle number
Current density = 0.5 A/g

Figure 4

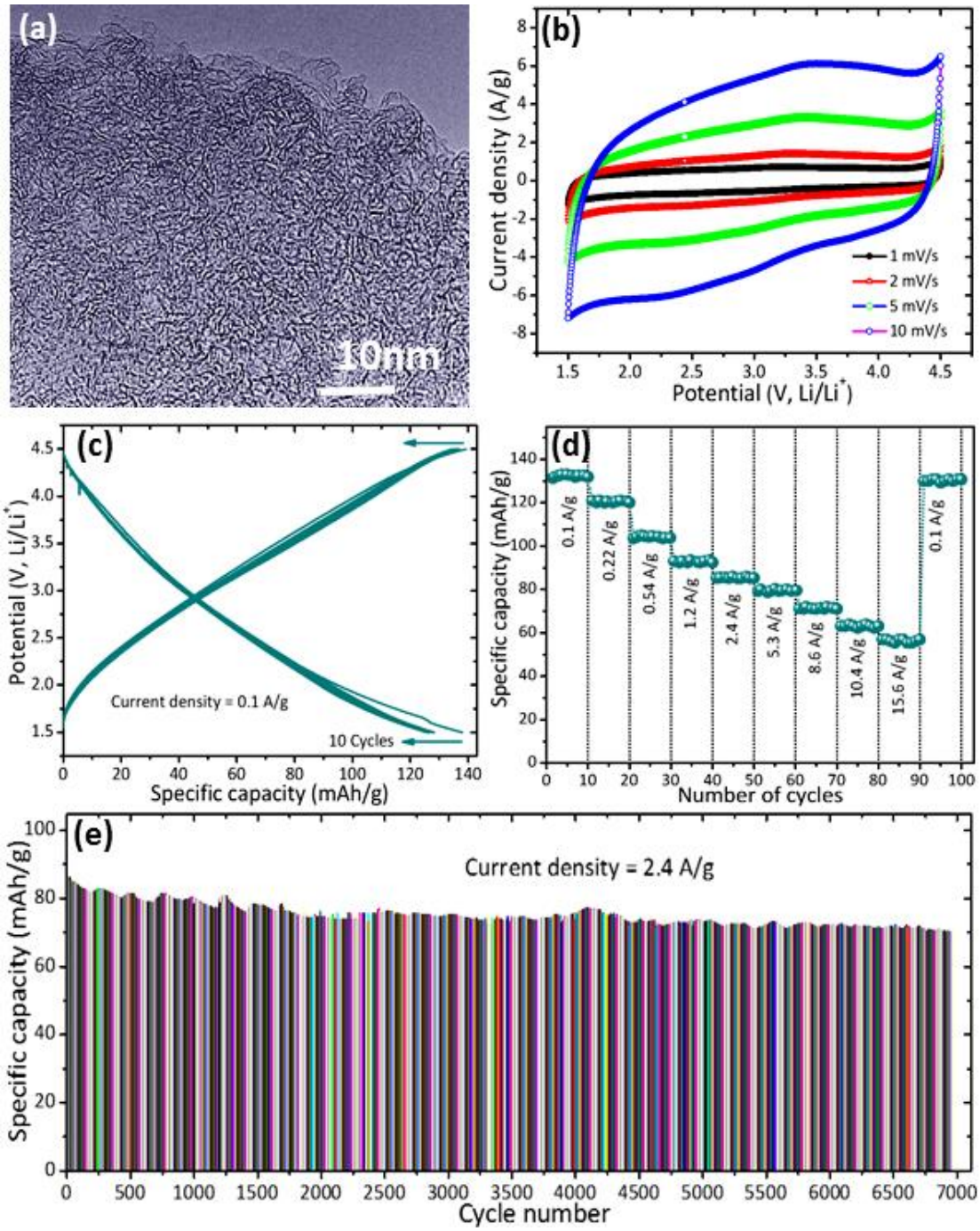
(a)
10nm
(b)
Current density (A/g)
Potential (V, Li/Li+)
1 mV/s
2 mV/s
5 mV/s
10 mV/s
(c)
Potential (V, Li/Li+)
Specific capacity (mAh/g)
Current density = 0.1 A/g
10 Cycles
(d)
Specific capacity (mAh/g)
Number of cycles
0.1 A/g
0.22 A/g
0.54 A/g
1.2 A/g
2.4 A/g
5.3 A/g
8.6 A/g
10.4 A/g
15.6 A/g
0.1 A/g
(e)
Current density = 2.4 A/g
Specific capacity (mAh/g)
Cycle number

Figure 5

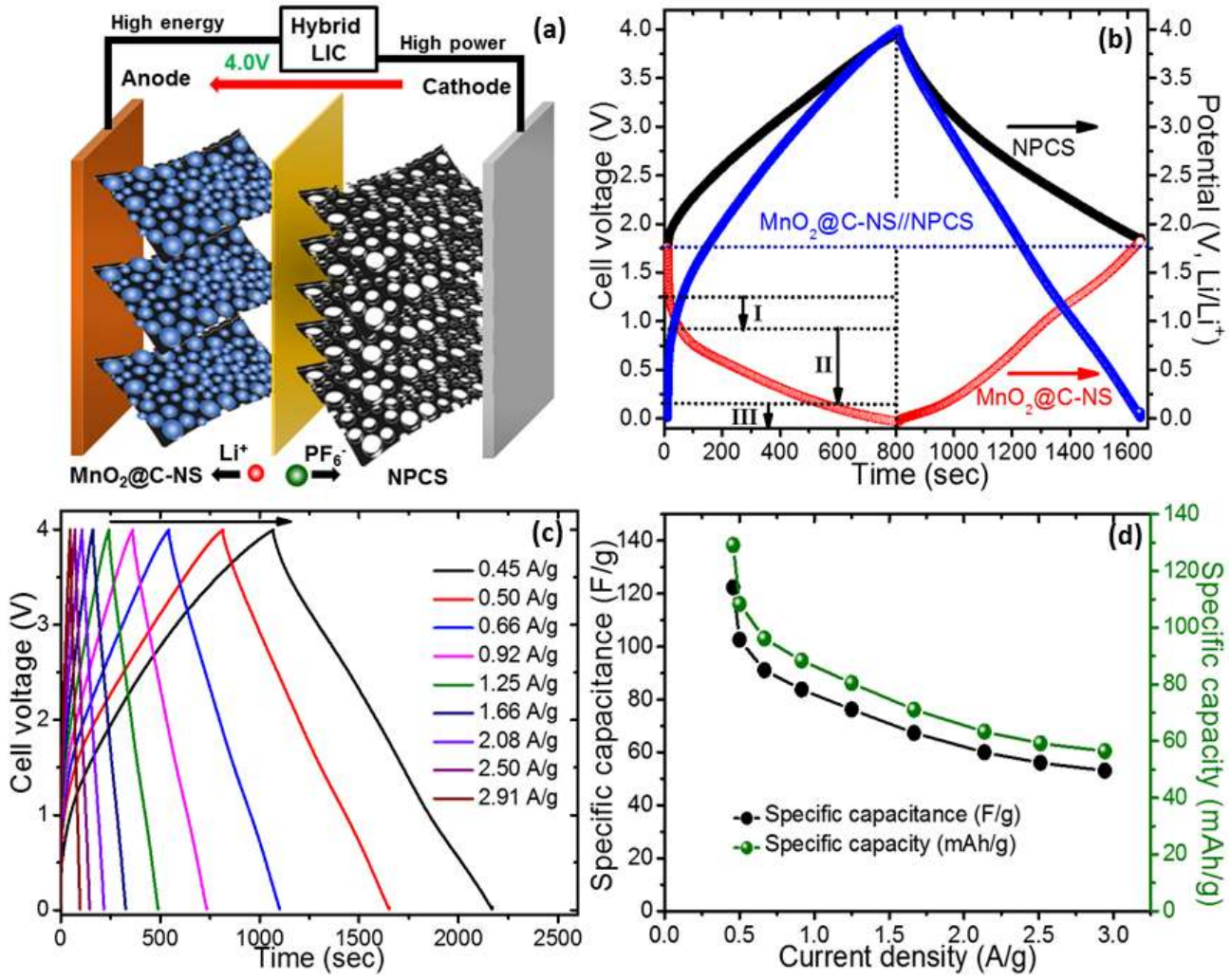
High energy
Hybrid LIC
High power
(a)
Anode
4.0V
Cathode
MnO2@C-NS
Li+
PF6-
NPCS
(b)
Cell voltage (V)
Potential (V, Li/Li+)
NPCS
MnO2@C-NS//NPCS
MnO2@C-NS
I
II
III
Time (sec)
(c)
Cell voltage (V)
0.45 A/g
0.50 A/g
0.66 A/g
0.92 A/g
1.25 A/g
1.66 A/g
2.08 A/g
2.50 A/g
2.91 A/g
Time (sec)
(d)
Specific capacitance (F/g)
Specific capacity (mAh/g)
Specific capacitance (F/g)
Specific capacity (mAh/g)
Current density (A/g)

Figure 6

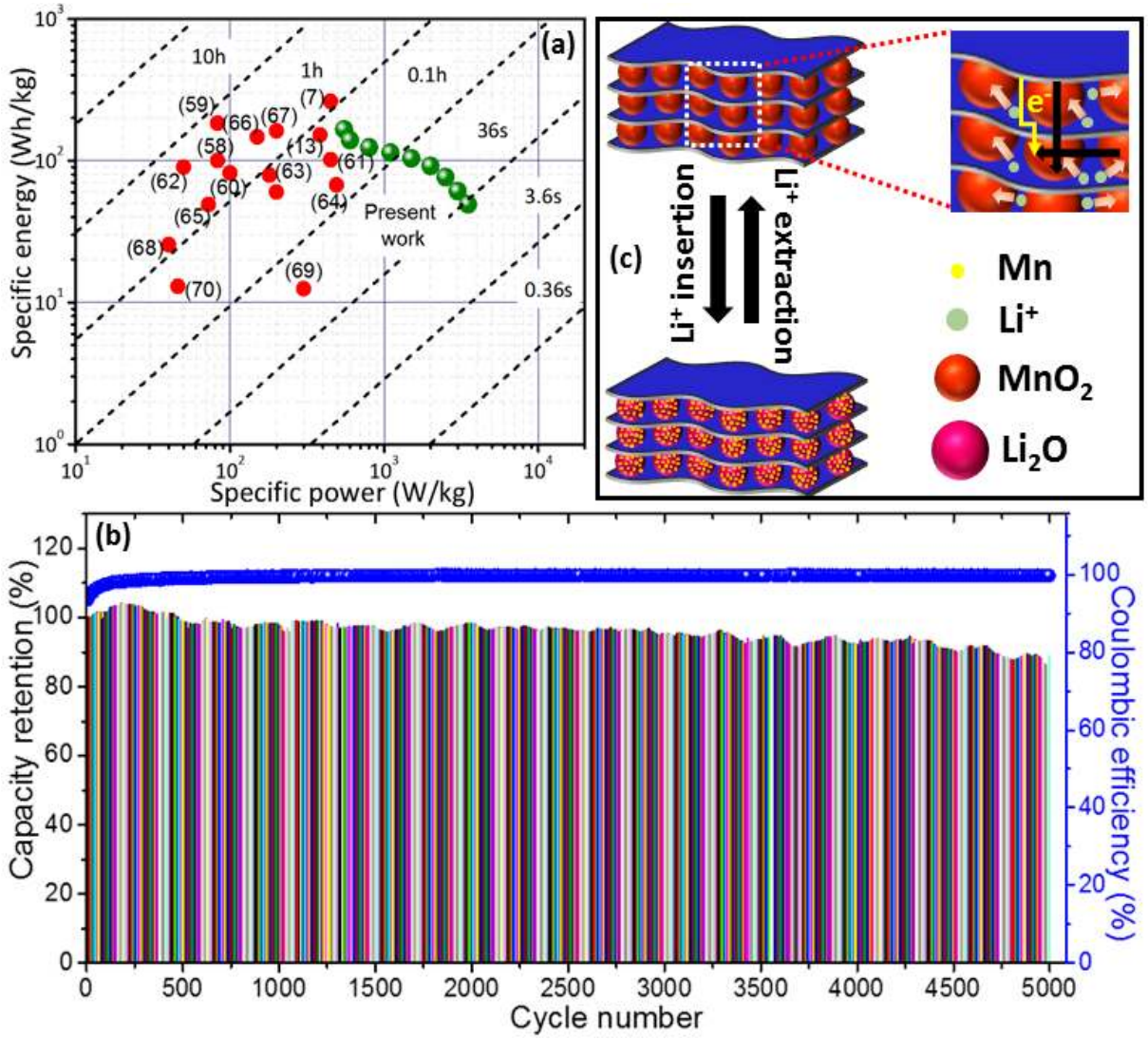
(a)
Specific energy (Wh/kg)
Specific power (W/kg)
10h
1h
0.1h
36s
3.6s
0.36s
Present work
(7)
(13)
(58)
(59)
(60)
(61)
(62)
(63)
(64)
(65)
(66)
(67)
(68)
(69)
(70)
(c)
Li+ insertion
Li+ extraction
e-
Mn
Li+
MnO2
Li2O
(b)
Capacity retention (%)
Coulombic efficiency (%)
Cycle number

The table of contents

Metal-Organic Framework (MOF) derived electrodes for high performance Li-Ion hybrid capacitor: Graphene-like nanosheets wrapped MnO_2 anode and Nanoporous carbon nanosheets cathode

Keywords MOF-derived elecctrodes, Manganese oxide, Nanoporous carbon, Li-ion capacitors, High energy density.

Deepak P. Dubal,[1,4*$] Kolleboyina Jayaramulu,[2,3*$] Sunil Janaky,[5] Štěpán Kment,[3] Pedro Gomez-Romero,[4] Chandrabhas Narayana,[5] Radek Zbořil[3*] and Roland A. Fischer[2*]

Metal Organic Framework (MOF) derived Electrodes with Robust and Fast Lithium Storage for Li-Ion Hybrid Capacitors

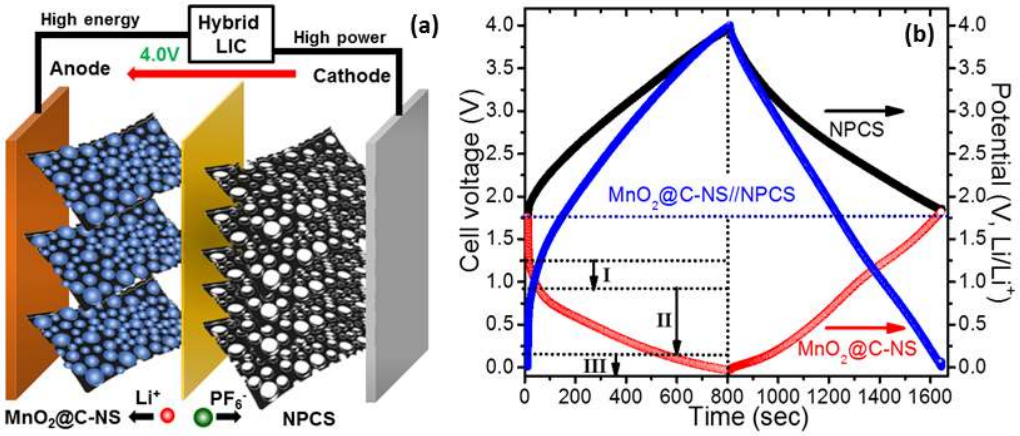

Supporting Information

Metal Organic Framework (MOF) derived Electrodes with Robust and Fast Lithium Storage for Li-Ion Hybrid Capacitors

Deepak P. Dubal,[1,4*$] Kolleboyina Jayaramulu,[2,3*$] Sunil Janaky,[5] Štěpán Kment,[3] Pedro Gomez-Romero,[4] Chandrabhas Narayana,[5] Radek Zbořil[3*] and Roland A. Fischer[2*]

[1]Dr. D. P. Dubal
School of Chemical Engineering, The University of Adelaide,
Adelaide, South Australia 5005, Australia
Email: dubaldeepak2@gmail.com

[2]Dr. K. Jayaramulu, Prof. Dr. R. A. Fischer
Chair of Inorganic and Metal-Organic Chemistry, Department of Chemistry and Catalysis Research Centre, Technical University of Munich, 85748 Garching, Germany
Email: jaya.kolleboyina@tum.de
Email: roland.fischer@tum.de

[3]Dr. K. Jayaramulu, Dr. S. Kment, Prof. Dr. R. Zboril
Regional Centre of Advanced Technologies and Materials,
Faculty of Science, Palacky University, Šlechtitelů 27, 783 71, Olomouc, Czech Republic.
Email: radek.zboril@upol.cz

[4]Dr. D. P. Dubal, Prof. Dr. P. Gomez-Romero
Catalan Institute of Nanoscience and Nanotechnology (ICN2), CSIC and the Barcelona Institute of Science and Technology, Campus UAB, Bellaterra 08193, Barcelona, Spain

[5]Prof. Dr. C. Narayana, Ms. S. Janaky
Chemistry and Physics of Materials Unit,
Jawaharlal Nehru Centre for Advanced Scientific Research (JNCASR)
Jakkur, Bangalore, 560064, India

[$]Both authors contributed equally.

Keywords: MOF-derived Materials, manganese oxide, nanoporous carbon, Li-ion capacitors, Energy Storage, Energy Density

Experimental and related aspects

Materials

All reagents and solvents were commercially available and used as supplied without further purification. $MnCl_2 \cdot 4H_2O$, 1,4-napthalenedicarboxylate, and KOH were obtained from Sigma-Aldrich.

Synthesis of $[Mn(1,4\text{-ndc})]_n$ (1):

The synthesis procedure of 1 has been described by Kitagawa et al.[1] Reaction of $MnCl_2 \cdot 4H_2O$ (1.0 mmol) with 1,4-napdcH_2 (1.0 mmol) and KOH (2.0 mmol) in water (10–12 ml) at 180 °C for 72h h resulted in pink colored powder in 40% yield with respect to Mn.

1. T. K. Maji, W. Kaneko, M. Ohba, S. Kitagawa, *Chem. Commun.* **2005**, 4613-4615.

Synthetic procedure for KMOF:

Nanocrystals of KMOF were prepared according to a slightly modified procedure from literature. **(ref) In** a 20 ml of Teflon, 1.51 g of BTC, 0.632 g of KNO_3, 0.074 g NH_4F of were dissolved in 15 mL of DMF under sonication. The autoclave was tightly closed and placed in an oven at 120 °C for 3 days. After cooling to room temperature, the supernatant was decanted and the products were washed three times with DMF, three times with methanol. Methanol as solvent was decanted and replaced once per day during the course of three days. Colorless rod crystals were recovered for KMOF in ≥90% yield based on potassium.

1. M. K. Kim, V. Jo, D. W. Lee, I.-W. Shim and K. M. Ok, *CrystEngComm*, **2010**, *12*, 1481-1484

Preparation of hybrid MnO2@carbon matrix

The composite material was prepared by the following method. The resultant MOF powder was heat treated in nitrogen flow of 100 ml per minute at 800 ºC with a heating rate of 5 ºC per minute for 6 h to carbonize the mixture. The resultant composite recovered after repetitive washing with ethanol and drying at 60 ºC.

Preparation of Nanoporous carbon sheets (NPS-800) from KMOF:

The nanoporous carbon sheets were prepared by the following method. . In a typical synthesis, 1 g of KMOF-1 prepared at a synthesis temperature of 120 °C. The KMOF-1 heated at 200 °C overnight. The activated KMOF-1 was heat-treated in a nitrogen flow of 100 ml per minute at 450 °C with a heating rate of 5 °C per minute for 6 h to carbonize the mixture. The resultant composite (denoted as NPS-450) have potassium-based impurities. Further, NPS-450 composite heat treated in a nitrogen flow of 100 mL per minute at various temperature 800 °C with a heating rate of 5 °C per minute for 8h. Finally, nanoporous carbon sheets (NPS-800) was recovered after dissolution of the potassium oxide in 5 wt% hydrochrloric acid, by filtration, repetitive washing with water/ethanol (1:1) and drying at 100 °C.

Materials characterization

The synthesized materials were characterized by different techniques. X-ray diffraction (XRD) data of all samples were collected by the X'Pert PRO PANanalytical equipment (Bragg-Brentano geometry with automatic divergence slits, position sensitive detector, continuous mode, room temperature, Cu-Kα radiation, Ni filter. The powder samples were dropped onto silicon wafer with grease and measured at the same equipment (5-80°, at a step of 0.0197°, with accumulation time 200 s per step). For Rietveld refinement, FullProf Suite program with VESTA graphical interface was used. The X-ray photoelectron spectra (XPS) analyses were obtained by X-ray photoelectron spectroscopy (XPS, SPECS Germany, PHOIBOS 150).The surface morphological analyses of samples were carried out using the different techniques such as field-emission scanning electron microscopy (FEI Quanta 650F Environmental SEM) and transmission electron microscopy (Tecnai G2 F20 S-TWIN HR(S) TEM, FEI). The Raman spectrum of respective sample were collected through instrument, DXR Raman (Thermo, USA); laser wavelength: 633 nm, laser power on sample: 2mW, exposition time: 5s, 32 spectra were averaged at each spot to obtain one data point. Adsorption studies of N_2 (77 K) of all samples were carried out using MICROMERITICS analyzer, outgassed at 423 K under high vacuum.

Electrochemical testing

Electrodes were prepared by mixing the active material (MnO2@C-NS or nanoporous carbon nanosehets NPS-800), Super-P conductive carbon black and polyvinylidene fluoride binder (PVDF) in an N-methyl-2-pyrrolidone (NMP) with 70 %:20 %:10% ratio. The resulting paste was uniformly coated onto Al or Cu foil, dried at 100 °C for 12 h, and pressed under hydraulic press. The mass loading of MnO2@C-NS and NPS-800 was around 1.5 mg/cm^2. Initially, both the materials MnO2@C-NS and NPS-800 were tested with half-cell configuration where the Li metal, glass-fiber and a 1 M lithium hexafluorophosphate in a 1:1 mixture of ethylene carbonate and dimethyl carbonate (1:1, EC:DMC) were used as counter electrode, separator and electrolyte, respectively. The NPS-800 cathode half-cell was tested within the voltage range from 4.5 to 1.5 V and MnO2@C-NS anode within 3.0 to 0.01 V using a Biologic potentio-galvanostat. Prior to assembling full LIC cell, MnO2@C-NS and NPS-800 were cycled 10 cycles in half-cells at 0.1 A/g, and then the cells were disassembled in the glove box and by collecting electrodes, full cell was fabricated and tested within 0.01 to 4 V. The $BiVO_4$ anode was fully discharged up to 0.01 V (vs. Li) before used in the full LIC cells. In present investigation, the mass ratio of MnO2@C-NS to NPS-800 O was maintained at 1:5 (1.6 mg of MnO2@C-NS and 7.9 mg of NPS-800).

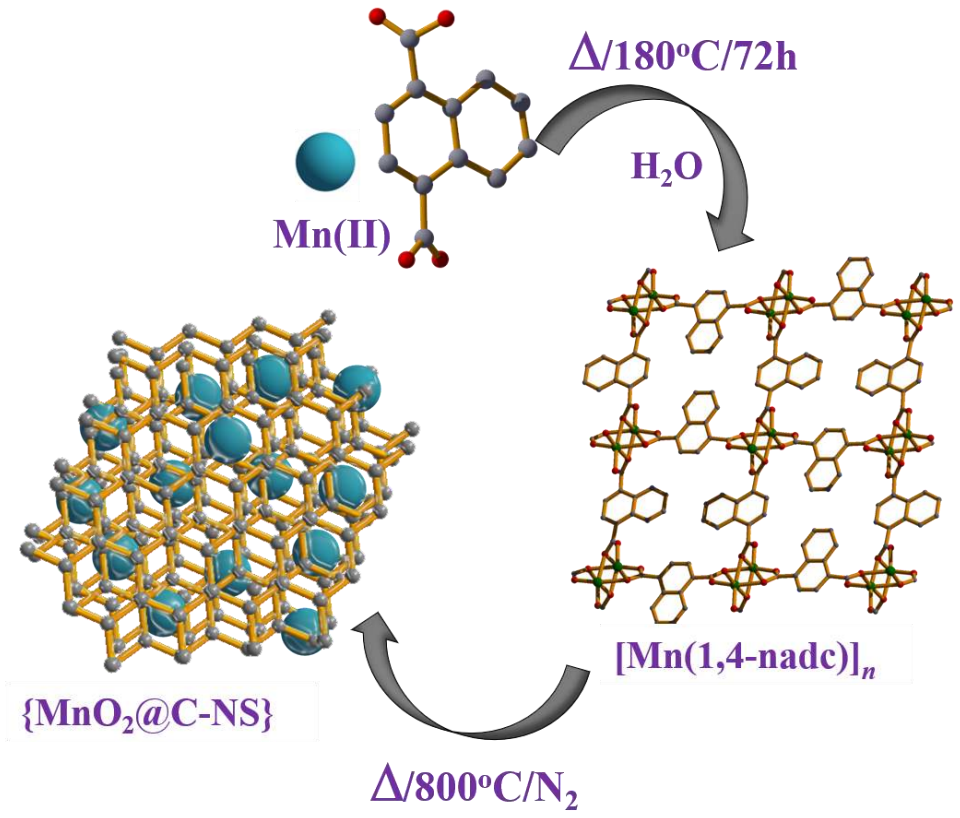

Figure S1. Synthesis concept of the step-wise formation of manganese nanoparticles at graphitic porous carbon matrix from manganese-based metal-organic framework

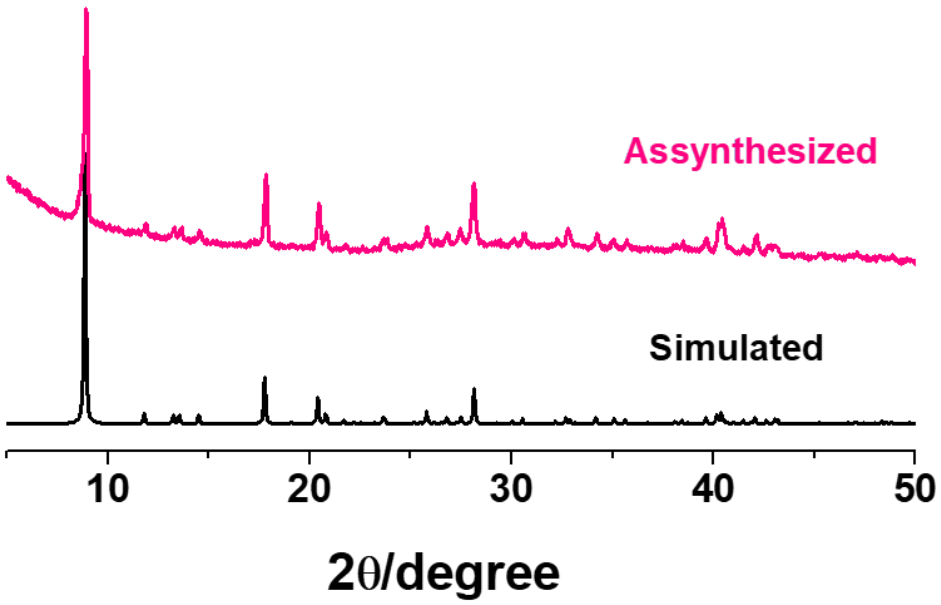

Figure S2 Powder XRD pattern of 1 (a) simulated pattern; (b) as-synthesized $[Mn(1,4\text{-napdc})]_n$ **(1)**

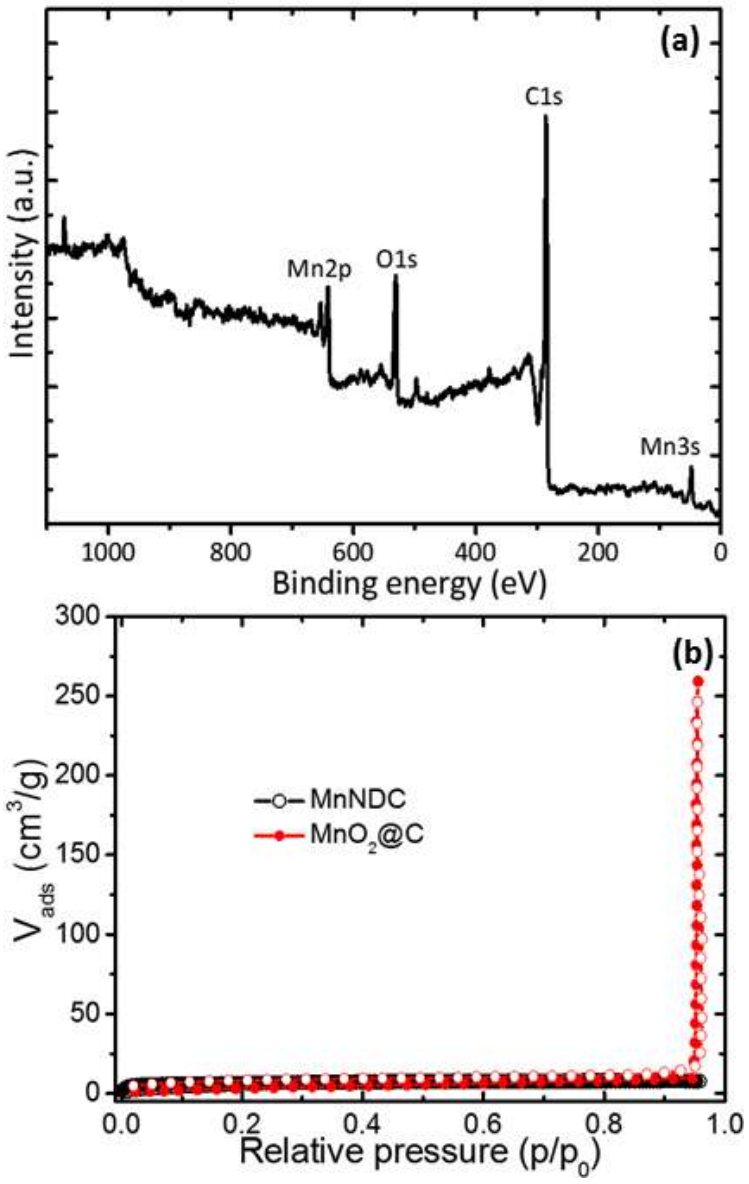

Figure S3 (a) Full XPS spectrum of **MnO_2@C-NS** nanocomposite suggesting the formation of MnO_2 and carbon. (b) Nitrogen adsorption/desorption isotherm of MnNDC and **MnO_2@C-NS**.

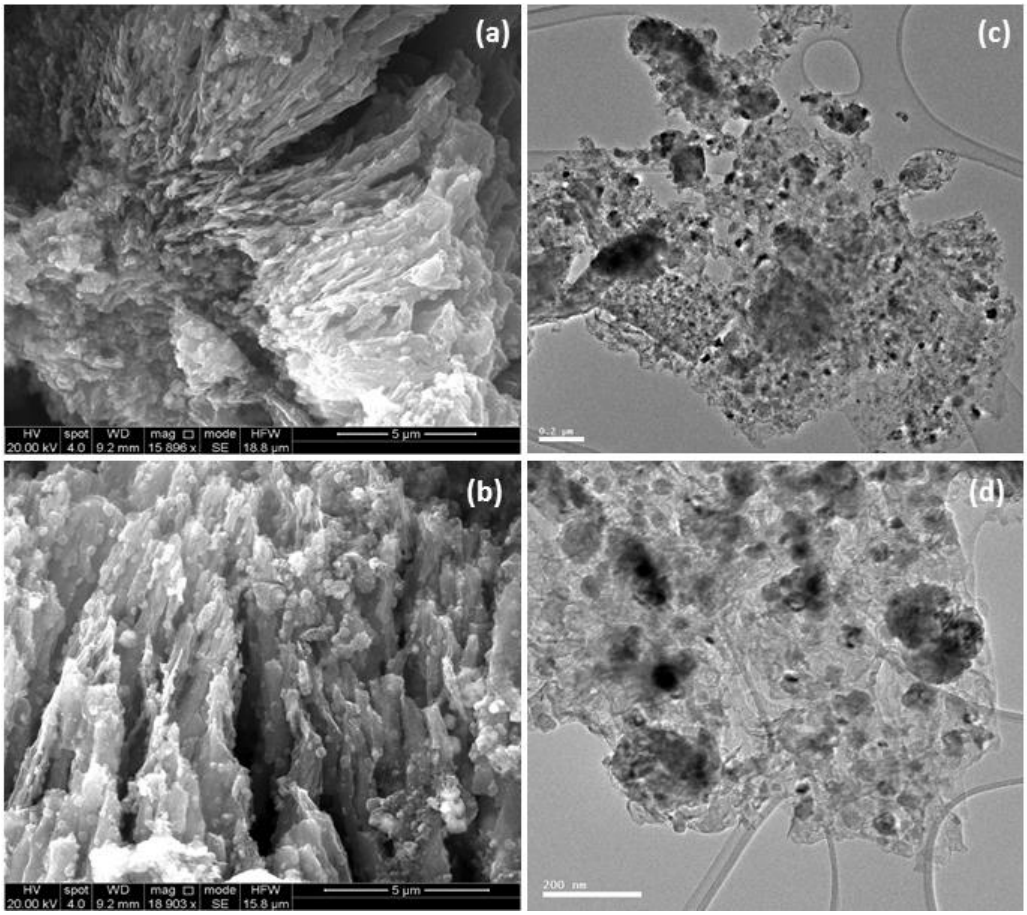

Figure S4 (a, b) SEM and (c, d) TEM images of MnO_2@C-NS at two different magnification confirming the formation of interleaved composite of graphene-like carbon nanosheets decorated with MnO_2 nanoparticles.

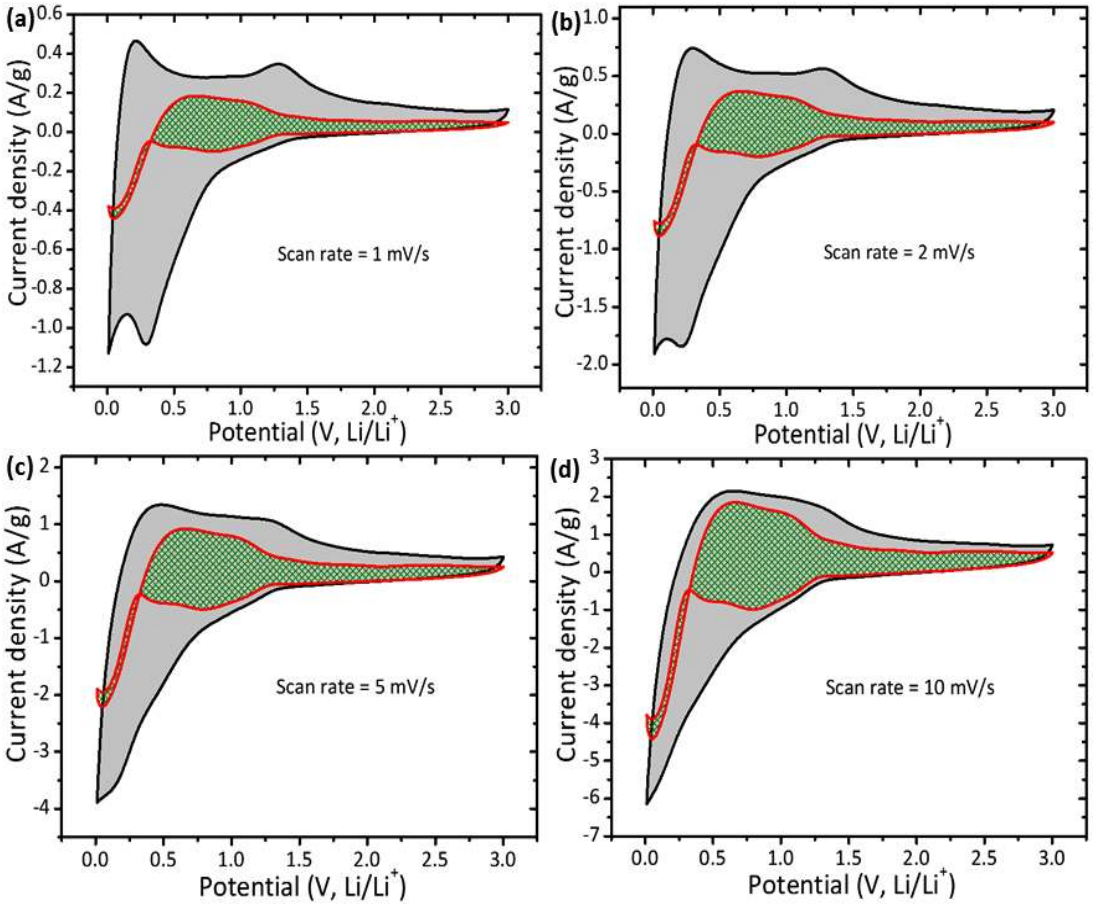

Figure S5 CV curves for MnO_2@C-NS at different scan rates with the capacitive contribution to the total current is shown by the shaded region, which suggest increasing trend of capacitive contribution with scan rate.

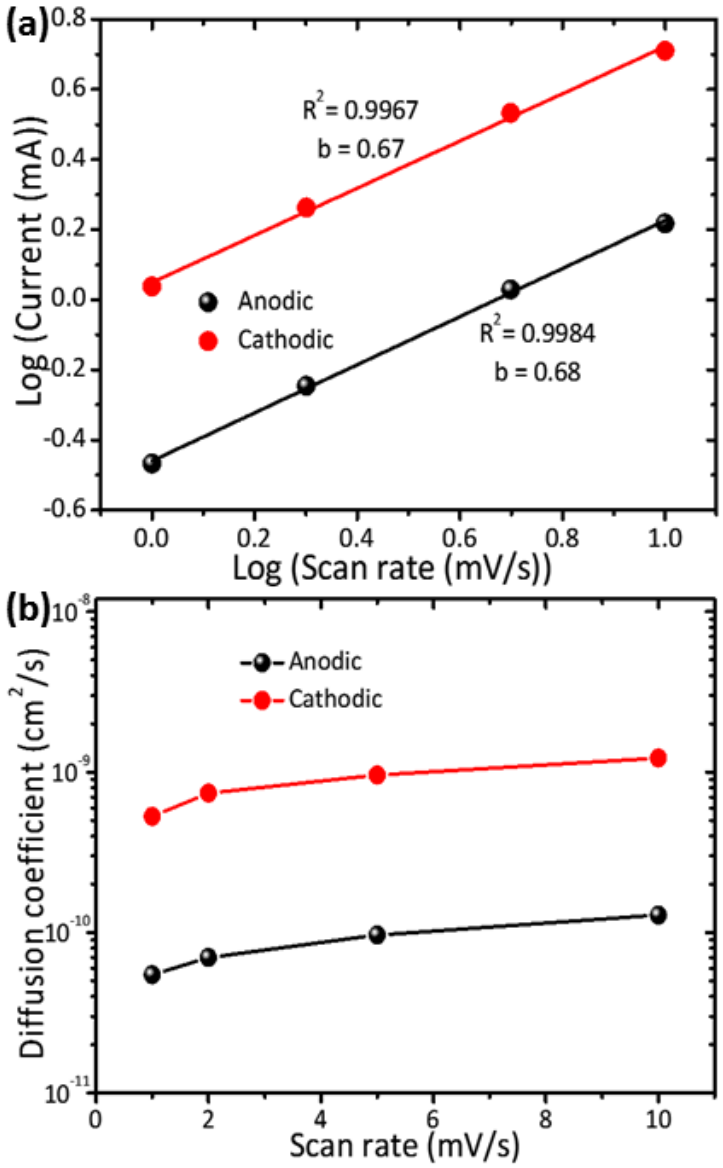

Figure S6 (a) Plot of log (current) vs log(scan rate) for anodic and cathodic responses. (b) Li-ion diffusion coefficients of MnO_2@C-NS electrode at different scan rates.

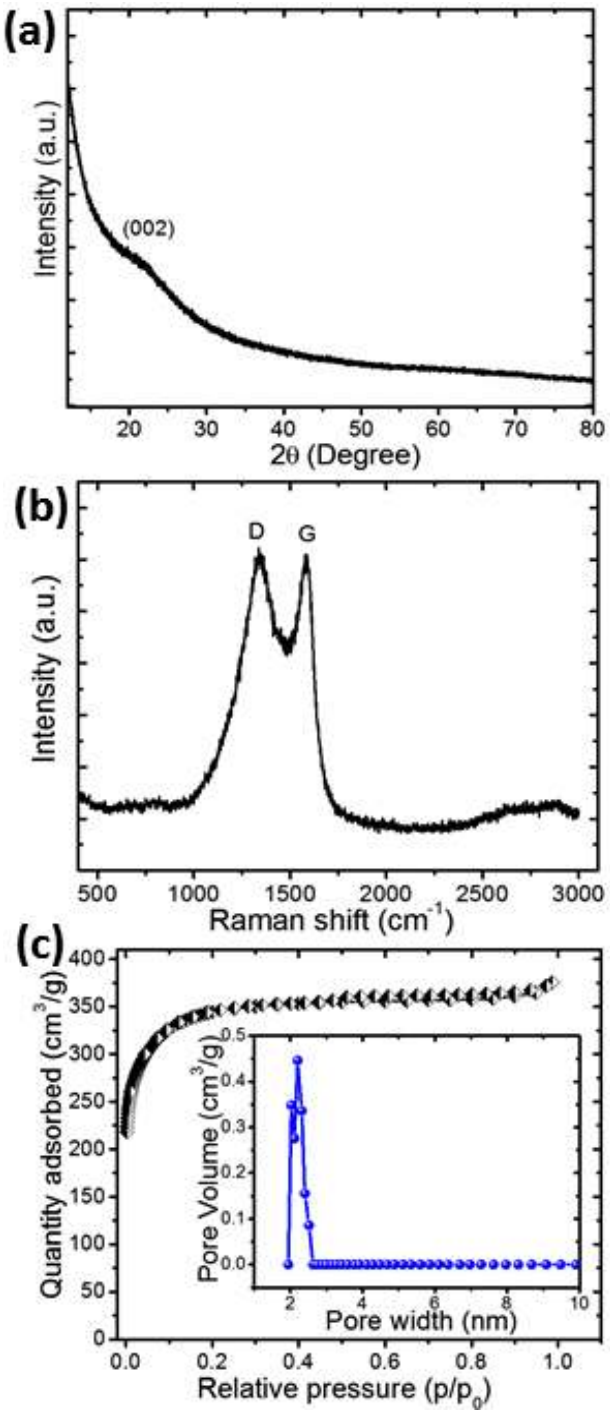

Figure S7 (a) XRD, (b) Raman and (c) BET analysis with corresponding pore size distribution curve (inset) for MOF-derived nanoporous carbon nanosheets (NPCS), confirming the formation of high surface area with tunable pore size NPCS cathode material.

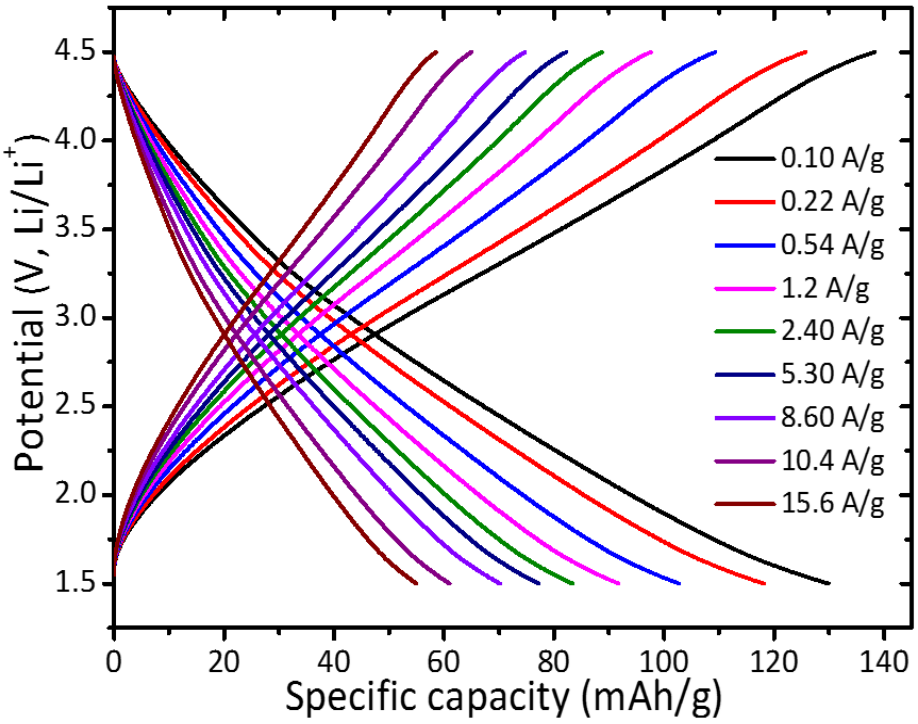

Figure S8 Galvanostatic charge/discharge curves for NPCS cathode in half cell configuration (vs Li/Li^+) at different current densities.

Supporting Information Table 1

Table 1 Comparison of electrochemical properties of carbon based anode materials with present report

Anode Material	Reversible capacity (mAh/g)	Capacity retention (mAh/g)	References
MnO_2@C-NS	1054 at 0.1 A/g	90 % at 0.5 A/g after 1000 cycles	Present work
MnO_2/carbon nanotube	820 at 200 mA/g	77 % at 200 mA/g after 50 cycles	[S1]
MnO_2/ Carbon Nanohorns	565 at 450 mA/g	98 % at 450 mA/g after 60 cycles	[S2]
Graphene-Wrapped MnO_2-Graphene Nanoribbons	890 at 0.1 A/g	24% increase after 245 cycles at 0.4 A/g	[S3]
MnO_2/carbon nanotube	500 at 50 mA/g	45 % at 50 mA/g after 16 cycles	[S4]
TiO_2-C/MnO_2	865 at 33.5 mA/g	90 % at 335 mA/g after 100 cycles	[S5]
MnO/C	798 at 200 mA/g	77 % at 200 mA/g after 40 cycles	[S6]
Graphene-MnO_2 Nanotube	581 at 100 mA/g	-	[S7]
Fe-MOF derived C-Fe_3O_4	975 at 100 mA/g	80 % at 100 mA/g after 50 cycles	[S8]
MOF derived ZnO quantum dots@hierarchically porous carbon	1200 at 75 mA/g	100 % at 75 mA/g after 50 cycles	[S9]

Supporting Information Table 2

Table 2 Comparison of published electrochemical properties of Li-ion capacitors with our present work

LIC cell	Energy density (Wh/kg)	Power density (W/kg)	Voltage (V)	Cycling stability	References
MnO_2@C-NS//NPCS	166 at 550 W/kg	3000 at 49 Wh/kg	4.0	91 % after 5000 cycles	Present work
N-CNPipes//PRGO	262 at 450 W/kg	9000 at 78 Wh/kg	4.0	89 % after 1000 cycles	[S10]
$Li_4Ti_5O_{12}$//AC	67.5 at 490 W/kg	4995 at 33.6 Wh/kg	3.0	85 % after 2000 cycles	[S11]
Li_3VO_4//AC	49.1 at 72.5 W/kg	24.5 at 129.7 Wh/kg	3.5	-	[S12]
Fe_3O_4-Graphene// 3D Graphene	147 at 150 W/kg	2587 at 86 Wh/kg	3.0	70 % after 1000 cycles	[S13]
Graphene-VN //carbon nanorods	162 at 200 W/kg	10000 at 64 Wh/kg	4.0	86% after 1000 cycles	[S14]
CNT/V_2O_5//AC	25.5 at 40 W/kg	6300 at 6.9 Wh/kg	2.7	80% after 10000 cycles	[S15]
TiO_2-B nanowire//CNT	12.5 at 300 W/kg	1300 at 8 Wh/kg	2.8	1000 cycles	[S16]
TiP_2O_7//AC	13 at 46 W/kg	370 at 0.2 Wh/kg	3.0	78% after 500 cycles	[S17]
$BiVO_4$//PRGO	152 at 384 W/kg	3861 at 42 Wh/kg	4.0	81% after 6000 cycles	[S18]

MnO-C//carbon nanosheets	100 at 83 W/kg	33650 at 21 Wh/kg	3.0	70 % after 5000 cycles	[S19]
3D-MnO/CNS//3D-CNS	184 at 83 W/kg	18000 at 83 Wh/kg	3.0	76 % after 5000 cycles	[S20]
HC//AC	82 at 100 W/kg	5500 at 45 Wh/kg	2.1	-	[S21]
TiC//PHPNC	101.5 at 450 W/kg	675000 at 23.4 Wh/kg	4.5	82 % after 5000 cycles	[S22]
Li-Hard carbon//AC	82 at 100 W/kg	50000 at 1 Wh/kg	2.8	100 % after 40 cycles	[S23]

References

[S1]	H. Xia, M. Lai, L. Lu, *J. Mater. Chem.*, **2010**, *20*, 6896
[S2]	H. Lai, J. Li, Z. Chen, Z. Huang, *ACS Appl. Mater. Interfaces* **2012**, *4*, 2325
[S3]	L. Li, A. R. O. Raji, J. M. Tour, *Adv. Mater.* **2013**, *25*, 6298
[S4]	A. L. M. Reddy, M. M. Shaijumon, S. R. Gowda, P. M. Ajayan, *Nano Lett.* **2009**, *9*, 1002
[S5]	J. Y. Liao, D. Higgins, G. Lui, V. Chabot, X. Xiao, Z. Chen, *Nano Lett.* **2013**, *13*, 5467
[S6]	B. Sun, Z. Chen, H. S. Kim, H. Ahn, G. Wang, *J. Power Sources* **2011**, *196*, 3346.
[S7]	A. Yu, H. W. Park, A. Davies, D. C. Higgins, Z. Chen, X. Xiao, *J. Phys. Chem. Lett.* **2011**, *2*, 1855
[S8]	M. Li, W. Wang, M. Yang, F. Lv, L. Cao, Y. Tang, R. Sun, Z. Lu, *RSC Adv.* **2015**, *5*, 356.
[S9]	S. J. Yang, S. Nam, T. Kim, J. H. Im, H. Jung, J. H. Kang, S. Wi, B. Park, C. R. Park, *J. Am. Chem. Soc.* 2013, 135, 7394-7397.
[S10]	D. P. Dubal, P. Gomez-Romero, *Mater. Today Energy* **2018**, *8*, 109.
[S11]	A. Jain, V. Aravindan, S. Jayaraman, P. S. Kumar, R. Balasubramanian, S. Ramakrishna, M. Srinivasan, M. P. Srinivasan, *Sci. Rep.* **2013**, *3*, 3002
[S12]	H. Y. Wei, D. S. Tsai, C. L. Hsieh, *RSC Adv.*, **2015**, *5*, 69176
[S13]	F. Zhang, T. Zhang, X. Yang, L. Zhang, K. Leng, Y. Huang, Y. Chen, *Energy Environ. Sci.*, **2013**, *6*, 1623.
[S14]	R. Wang, J. Lang, P. Zhang, Z. Lin, X. Yan, *Adv. Funct. Mater.* **2015**, *25*, 2270
[S15]	Z. Chen, V. Augustyn, J. Wen, Y. Zhang, M. Shen, B. Dunn, Y. Lu, *Adv. Mater.* **2011**, *23*, 791.
[S16]	Q. Wang, Z. Wen, J. Li, *Adv. Funct. Mater.* **2006**, *16*, 2141
[S17]	V. Aravindan, M. V. Reddy, S. Madhavi, S. G. Mhaisalkar, G. V. Subba Rao, B. V. R. Chowdari, *J. Power Sources* **2011**, *196*, 8850
[S18]	D. P. Dubal, K. Jayaramulu, R. Zboril, R. A. Fischer, P. Gomez-Romero, *J. Mater. Chem. A*, **2018**, *6*, 6096
[S19]	Y. Zhao, Y. Cui, J. Shi, W. Liu, Z. Shi, S. Chen, X. Wang, H. Wang, *J. Mater. Chem. A*, **2017**, *5*, 15243
[S20]	H. Wang, Z. Xu, Z. Li, K. Cui, J. Ding, A. Kohandehghan, X. Tan, B. Zahiri, B. C. Olsen, C. M. Holt and D. Mitlin, *Nano Lett.*, **2014**, *14*, 1987-1994.

[S21]	W. J. Cao and J. P. Zheng, *J. Power Sources*, **2012**, *213*, 180
[S22]	H. Wang, Y. Zhang, H. Ang, Y. Zhang, H. T. Tan, Y. Zhang, Y. Guo, J. B. Franklin, X. L. Wu, M. Srinivasan, H. J. Fan and Q. Yan, *Adv. Funct. Mater.*, **2016**, *26*, 3082
[S23]	W. J. Cao, J. P. Zheng, *J. Power Sources* **2012**, *213*, 180